

Magnesium-Titanium nanoparticles by gas phase synthesis for hydrogen storage purposes

A Transmission Electron Microscopy study

By Sytze de Graaf

First supervisor:
Prof. dr. ir. B.J. Kooi

Second supervisor:
Prof. dr. G. Palasantzas

Zernike Institute for Advanced Materials
University of Groningen

September 27, 2016

Abstract

Magnesium is a possible candidate for solid state hydrogen storage due to its light weight and low material costs. However, its hydrogen sorption cycling performance is limited by the high thermodynamic stability of magnesium hydride and its poor kinetic properties. These properties can be altered by downscaling from bulk to nanostructured magnesium. Gas phase synthesized magnesium nanoparticles offer a possible storage system, but suffer from oxidation and magnesium evaporation owing to the high reactivity of magnesium. Alloying with titanium not only prevents the latter problems, but also gives the opportunity to improve hydrogen sorption properties. This bimetallic system shows the strength of nanotechnology where out-of-equilibrium materials can be produced, as magnesium and titanium are immiscible in bulk but turn out to be miscible in nanoparticles. In this thesis magnesium titanium nanoparticles and their performance as a solid state hydrogen storage medium are characterized by transmission electron microscopy. The nanoparticles are synthesized with a high pressure magnetron sputtering system, which gives control over the nucleation and growth conditions. A stable nucleation rate could only be sustained by introducing hydrogen or methane gas in the system. Consequently, titanium reacts readily with the elements in the gas which impacts the nanoparticle growth. Small nanoparticles below 25 nm are greatly affected by magnesium oxidation, leading to void development which imposes a bottom limit to the nanoparticle's size. Hydrogen absorption and magnesium evaporation are competing processes of which the latter can be suppressed by quick absorption within two hours at 250 °C. The crystal structure of the hydride can be tuned from a rutile to a fluorite structure by altering the composition. However, regardless of composition, size, crystal structure, structural motif and shape, no hydrogen is desorbed even at 400 °C in high vacuum conditions. As such gas phase synthesized magnesium titanium bimetallic nanoparticles are in their present forms not a suitable candidate for solid state hydrogen storage.

Table of Contents

1. Introduction.....	4
1.1 Hydrogen economy.....	4
1.2 Magnesium nanoparticles as a solid state hydrogen storage medium	7
1.2.1 Kirkendall effect in magnesium nanoparticles.....	7
1.2.2 Bimetallic magnesium nanoparticles.....	7
1.2.3 Magnesium-Titanium nanoparticles.....	8
2. Theory.....	9
2.1 Metal hydrides	9
2.1.1 Thermodynamics and kinetics of metal hydrides	9
2.2 High pressure magnetron sputtering.....	13
2.2.1 Inert gas condensation: Nucleation and growth.....	13
3. Experimental procedures	15
3.1 Nanoparticle cluster source	15
3.2 Hydrogenation experimental setup	16
3.3 TEM characterization with JEOL 2010 and JEOL 2010F.....	16
4. Results and discussion	19
4.1 Nucleation rate control of Mg-Ti nanoparticles stimulated by CH ₄ and H ₂ gas.....	19
4.2 Nucleation and growth of Mg-Ti nanoparticles: The effect of the gas environment.....	20
4.2.1 Synthesis in an Ar gas environment	20
4.2.2 Synthesis in an Ar-CH ₄ gas environment.....	24
4.2.3 Synthesis in an Ar-H ₂ gas environment.....	28
4.2.4 Oxidation associated Kirkendall effect	32
4.3 Hydrogenation of Mg-Ti nanoparticles	34
4.3.1 Thermal competition of hydride formation and Mg evaporation	34
4.3.2 Influence of Ti concentration on the hydride crystal structure	39
4.3.3 Surface nucleation of Copper nanoparticles	42
4.4 Dehydrogenation of Mg-Ti-H nanoparticles	43
5. Conclusions.....	47
6. Future research and recommendations	49
Acknowledgements.....	51
Appendix.....	52
References.....	54

1. Introduction

1.1 Hydrogen economy

Global population growth causes an exponential energy demand which is predominantly supplied by fossil fuels such as oil, gas and coal. At present, the fossil fuel reserves are steadily increasing [1], however the resources are limited in nature. Depending on the scenario, the oil, gas and coal production will peak approximately in 2050, followed by depletion of the reserves in the future decades [1]. The ever increasing demand and decreasing availability directly impacts the costs in the near future, hence the scarcity threatens the energy and economic stability worldwide [2]. Furthermore the production and consumption of fossil fuels poses an immediate threat to the global environment by the emission of greenhouse gases (mainly carbon dioxide (CO₂), nitrogen oxides (NO_x) and methane (CH₄)). As a result the CO₂ concentration, which is the dominant greenhouse gas, continues to rise at an increasing rate leading to a global temperature rise that is considered a high risk if it exceeds 2 °C, which will be reached by 2050 at the current pace [1], [3], [4]. The transition to renewable energy is of high priority as the current leading energy resources are depleting and the global environment is highly affected by the use of fossil fuels.

In 2014 around 86% of the total energy demand was supplied by fossil fuels and the remaining 14% by renewable energy sources as shown in Table 1. In order to limit the global temperature rise, a 75% reduction in CO₂ emission is required by 2050 accompanied with an increase of renewable energy sources [3]. A promising initiative is 20% renewable power by 2020, 50% by 2050 and fully converted to 100% by 2100 [1]. Taking the contribution of 23%, and growing, CO₂ emission due to transport into account, it is evident that renewable energy sources should have the possibility to be stored on-board in a compact, light and safe manner.

Source	2012 (GTOE)	2013 (GTOE)	2014 (GTOE)	2014 % Share
Oil	4.1389	4.1851	4.2313	32.60
Gas	2.9863	3.0204	3.0545	23.53
Coal	3.7237	3.8267	3.9297	30.27
Nuclear	0.5599	0.5632	0.5665	4.36
Hydro	0.8336	0.8568	0.8800	6.78
Renewables	0.2408	0.2793	0.3178	2.45
Total	12.4832	12.7304	12.9798	100

Table 1: Primary energy consumption by fuels in Giga tons of oil equivalents (GTOE) [1].

Hydrogen is a good alternative to replace fossil fuels, since it is considered a clean energy carrier. Essentially there are two methods to use hydrogen as fuel for mobile applications. First, hydrogen can be burned with oxygen in a conventional combustion engine which can achieve higher efficiencies (around 25%) than typical hydrocarbons. When hydrogen is burnt with oxygen the only product or exhaust gas is H₂O, however when burnt with air, nitrogen oxides can be formed. The second method uses a hydrogen fuel cell, which produces electricity by the electron transfer process from oxygen to hydrogen and can reach efficiencies over 50% which can be utilized as a power source for hybrid electric vehicles [4], [5].

Additionally hydrogen is the most abundant element in the universe, but not commonly found in the pure form. On earth the majority of hydrogen is found in the form of H₂O. The chemical energy per electron is the highest for hydrogen among all elements in the periodic table since the element consists of only one proton surrounded by one electron. The specific chemical energy of hydrogen is at least three times larger (142 MJ kg⁻¹) than that of conventional fossil fuels like liquid hydrocarbons (47 MJ kg⁻¹), e.g. the energy content of 9.5 kg hydrogen is equivalent to 25 kg gasoline [4]. On the contrary, the main drawback of hydrogen is the low volumetric energy density which is a serious obstacle that hinders implementation of hydrogen fuel for automotive applications. For instance, at ambient conditions hydrogen exists as H₂ in a molecular gas having a low density of 0.08988 kg m⁻³ e.g. 9.5 kg of hydrogen gas occupies a volume of 106 m³, not practical in any way [5].

Hydrogen storage systems can be categorized in three main groups:

1. High-pressure hydrogen gas cylinders
2. Liquid hydrogen cylinders
3. Solid state storage

High-pressure gas cylinders are the most common storage systems for hydrogen, in which hydrogen is compressed to 200 bar. For more sophisticated high-pressure systems the pressure can reach 800 bar, increasing the volumetric density to 36 kg m⁻³ which comes at the cost of decreasing gravimetric density as thicker walls are required to withstand the high pressure [6], [7]. Liquid hydrogen is stored in cryogenic tanks having a volumetric density of 70.8 kg m⁻³. The low critical point of 33 K imposes technical difficulties to ensure hydrogen remains a liquid. Therefore, liquid hydrogen is stored in open systems to prevent tremendous pressure increase. Besides, liquefaction of hydrogen gas costs a sincere amount of energy which reduces the overall efficiency of the storage method [6].

The last category consists of materials that can adsorb hydrogen on the surface, or absorb hydrogen inside the material. In the former case hydrogen is weakly bound (0.01 – 0.1 eV) at a distance of roughly one molecular radius from the surface via van der Waals interactions and is called physisorption. Since physisorption is a surface phenomenon, the maximum quantity of adsorbed hydrogen is one monolayer which corresponds to 1.3x10⁻⁵ mol m⁻². Considering the weak interaction and limited adsorption capacity, physisorption of hydrogen is only observed at low temperatures and the highest capacity is reached for high surface to volume materials like graphene, carbon nanotubes and nanostructured graphite. On the other hand hydrogen can be absorbed inside a metal after being physisorbed. The sequence of this process is initiated by dissociating physisorbed molecular hydrogen into two charge neutral hydrogen atoms. Followed by absorption in the material to form a solid metal hydride which can achieve volumetric densities of 110 kg m⁻³ [5], [6], [4].

Storage Parameter	2020
System gravimetric capacity	1.8 kWh/kg (5.5 wt%)
System volumetric capacity	1.3 kWh/L (0.040 kg H ₂ /L)
Storage system cost	10 \$/kWh (333 \$/kg H ₂)

Table 2: Targets for 2020 by the Department of Energy (DOE) of the USA for onboard hydrogen storage for Light-Duty Fuel Cell Vehicles.

As a guide for scientific work on the field of metal hydrides for hydrogen storage, the US Department of Energy (DOE) specifies targets for commercially viable hydrogen storage systems as shown in Table 2. The volumetric density of metal hydrides is significantly higher than in the case of high-

pressure cylinders or liquefied hydrogen. Furthermore metal hydrides provide a safe technique of storage in contrast to the more common storage methods. However, the intrinsic gravimetric density is the general weakness of metal hydrides which is in the range of 2-10 wt%. Overall metal hydrides are considered a convenient method for hydrogen storage. From an application point of view, the most important characteristics for hydrogen storage in metal hydrides are [8]:

- Hydrogen storage capacity
- Thermal stability of the hydride
- Hydride sorption kinetics
- System costs

Magnesium (Mg) is an attractive option that has been studied extensively as a potential hydrogen storage system, as it meets two important storage criteria: high storage capacity and relatively inexpensive. Mg can absorb 7.6 wt% hydrogen which meets the DOE target for 2020, and it's abundantly available on earth such that it's inexpensive compared to other metals. The major drawbacks of Mg are the poor hydrogenation kinetics and the high thermal stability of Mg hydride [5]–[8].

Nanostructured Mg offers the possibility to circumvent these issues as the thermodynamics and kinetics can be altered in these systems. Nanostructured materials are typically used to improve kinetics of a system owing to the high surface to volume ratio. Additionally, finite size effects start to play a role as soon as the size of the nanostructured material is comparable with a characteristic length scale of the system. When the size of nanostructured Mg is reduced until roughly 1.3 nm, finite size effects start altering the thermodynamics of hydrogen absorption stability according to Hartree-Fock and Density Functional Theory (DFT) calculations [9]. In this case the Mg hydride is destabilized when fewer than 19 Mg atoms are present per cluster. However, typically these extremely small clusters are very difficult to achieve in practice. Bottom-up synthesis of Mg nanoparticles offers great control over the characteristics of the system and therefore has the opportunity to control the structure-property relation.

1.2 Magnesium nanoparticles as a solid state hydrogen storage medium

1.2.1 Kirkendall effect in magnesium nanoparticles

Earlier work of Krishnan *et al.* has shown that pure Mg nanoparticles synthesized with high pressure magnetron sputtering suffer from the Kirkendall effect that gives rise to loss of Mg [10]. The Kirkendall effect is described as a net mass flux compensated by a vacancy flux over an interface by atomic diffusion through vacancy exchange, as a consequence of imbalanced diffusion coefficients [11]. For Mg nanoparticles two mechanisms of the Kirkendall effect were ascribed to oxidation and evaporation of Mg. Mg nanoparticles oxidize even in an Ultra-high vacuum (UHV) environment. Oxidation results in a magnesium oxide (MgO) shell around the nanoparticle which reaches, at relatively low temperatures, a diffusion limited thickness of 3-4 nm. During MgO shell growth the imbalance in diffusion constants of magnesium anions and oxygen cations gives rise to an inward vacancy flux. Consequently, vacancies cluster as the vacancy density increases at the interface ultimately leading to void formation [12]. As long as sufficient Mg is available for MgO growth, the MgO thickness is independent of nanoparticle size. This implies that Mg consumption increases significantly for smaller nanoparticles e.g. pure non-hollow Mg nanoparticle with only an MgO shell smaller than 10 nm cannot be produced with high pressure gas phase synthesis.

The latter Kirkendall effect is observed during vacuum annealing of Mg nanoparticles. When heating at 300 °C in vacuum (10^{-7} mbar) void formation is heavily dependent on Mg nanoparticle size e.g. nanoparticles in the range of 15-20 nm and 20-50 nm are completely hollow in 1 hour and 5 hours, respectively. This effect has been attributed to thermodynamically driven evaporation of Mg to reach its equilibrium vapour pressure. According to the Kelvin equation the equilibrium vapour pressure is proportional to the surface curvature:

$$\ln \frac{p}{p_0} = \frac{4\gamma V_m}{dRT} \quad (1)$$

Where p is the particle's vapour pressure, p_0 the vapour pressure of a flat surface, γ the surface energy, V_m the particle's molar volume, R and T are the gas constant and the temperature, and d is the particle's diameter. Hence the thermodynamic driving force for evaporation is many orders of magnitude higher for nanoparticles of 10 nm compared to nanoparticles of 50 nm. The hydrogenation sequence of Mg nanoparticles is performed by heating to 250 °C in a hydrogen gas atmosphere. Also under these conditions void formation due to Mg evaporation cannot be prevented. This effect demonstrates the pitfall of the bottom-up approach of gas phase synthesis of Mg nanoparticles for hydrogen storage with high pressure magnetron sputtering. Long-time thermal stability is one of the major required features for reversible hydrogen storage and thus cannot be offered by these Mg nanoparticles.

1.2.2 Bimetallic magnesium nanoparticles

Bimetallic Mg-rich nanoparticles are considered a good solution to minimize void formation due to the Kirkendall effect. Besides aiding the stability of the nanoparticles, the additional metal can be functionalized i.e. forming a bimetallic system that can have a multitude of chemical and physical properties that is different from the two isolated elements, based on its size, structure and composition. DFT calculations have shown that transition metals act as catalysts for molecular hydrogen dissociation when doped in Mg [13]. Furthermore, bimetallic Mg-rich nanoparticles have

the possibility to form a hydride crystal structure that has improved thermodynamic and kinetic properties compared to pure Mg nanoparticles [14].

Even though it is typically difficult to gain control over the nucleation and growth of gas phase synthesized bimetallic nanoparticles, it has been demonstrated that it is possible to tune the structure and composition of the nanoparticles [15], [16]. Magnesium has been alloyed with several different materials to form bimetallic nanoparticles e.g. Cu, Ni, Ti. For these three systems void development is completely suppressed which was attributed to the reduced vapour pressure induced by the alloyed structure and the rapid formation of a stable hydride. The former two alloys are affected by phase segregation after hydrogenation originating from the formation enthalpy of the hydrides, enhanced atomic mobility and surface energy [16]. This is not a favourable phenomenon, as it is the alloyed crystal structure that prevents Mg evaporation during (de)hydrogenation. Remarkably, no phase separation was observed in the Mg-Ti nanoparticles [16], which is a promising indication for a robust reversibly system for hydrogen storage.

1.2.3 Magnesium-Titanium nanoparticles

For the last years, many research groups have shown interest in Mg-Ti for hydrogen storage. Particularly nanostructured systems such as nanocrystalline magnesium produced by means of ball milling [17]–[19], thin films and thin film multilayer stacks [20]–[23] and nanoparticles [24]–[26] have been studied. The aim of these studies is to reduce the stability of magnesium hydride to achieve hydrogen desorption at lower temperature and to improve hydrogen sorption kinetics. Generally for these nanostructured systems the thermodynamic stability is slightly decreased, whereas the kinetics of hydrogen uptake and release are affected more prominently. Several theories have been suggested to explain the reduced stability of the hydride Mg-Ti thin films on the basis of interfacial energy and elastic clamping [20], [21].

Alloying Mg and Ti is a remarkable phenomenon as the system has a positive enthalpy of mixing i.e. phase separation is thermodynamically favourable. Only a very small concentration of Ti can be dissolved in equilibrium in Mg and vice versa. No intermetallic is formed such that it is not possible to produce an Mg-Ti alloy in bulk [27]. This emphasises the strength of nanostructured materials where new structures different from bulk material can be synthesized by an out-of-equilibrium synthesis method. It is the thermodynamic instability of the Mg-Ti alloy that lies at the basis of the theories that explain the properties of the Mg-Ti alloyed nanostructured systems. Hence, the coupling of the two materials in a metastable system gives rise to interesting properties that could enhance hydrogenation characteristics.

2. Theory

2.1 Metal hydrides

Metals can absorb relatively large amounts of hydrogen, which form several structures depending on the concentration of hydrogen. Initially, physisorbed hydrogen molecules dissociate on the surface followed by atomic hydrogen (H) diffusion through the metal (M). At low concentrations ($H/M < 0.1$) the metal dissolves a small amount of hydrogen as a solid solution (α -phase), expanding the metal lattice by approximately $2-3 \text{ \AA}^3$ per hydrogen atom. For these low concentrations the hydrogen is sparsely distributed in the host metal, such that H-H interactions are negligible. For increased hydrogen concentration ($H/M > 0.1$) the H-H interactions become locally important as a consequence of the lattice expansion, causing nucleation of the metal hydride (β -phase). In the β -phase the hydrogen resides at specific sites (e.g. tetrahedral or octahedral sites) in the metal lattice and in many cases this is accompanied with a substantial volume expansion of 20-30% with respect to the pure metal. For a large intermediate region of hydrogen concentration the α -phase and β -phase coexist, followed by the pure β -phase for higher hydrogen concentrations [28]. A schematic illustration is shown in Figure 1.

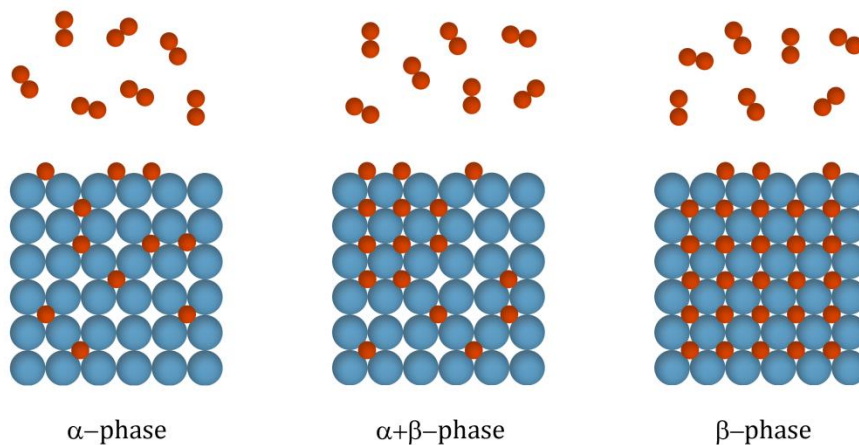


Figure 1: A schematic representation of the formation of the three states (with two phases) during hydrogen absorption.

2.1.1 Thermodynamics and kinetics of metal hydrides

The general chemical reaction formula for the formation of a metal hydride is $M + H_2 \rightleftharpoons MH_2 + \Delta H$, where M and MH_2 denote the metal and the metal hydride, respectively. And ΔH is the heat of formation, or the formation enthalpy. This quantity corresponds to the amount of heat absorbed or liberated during the formation of the metal hydride. Depending on the metal, the heat of formation can be either positive or negative corresponding to an exothermic and endothermic reaction, respectively. However, in most cases the hydrogenation of the metal is an exothermic reaction, i.e. heat is released. Accordingly, the reverse reaction corresponding to the desorption of hydrogen is endothermic requiring the same amount of heat to be supplied.

A standard method to reveal thermodynamic properties of a metal hydride system is a pressure-composition isotherm (PCI) as depicted in Figure 2. In a PCI the equilibrium hydrogen gas pressure is plotted versus the hydrogen concentration for several temperatures. It provides information regarding the present phases and the thermal stability. As previously discussed, a solid solution is formed for low hydrogen concentration, followed by a coexistence region and ultimately the pure hydride phase. In the α -phase the hydrogen concentration strongly depends on the hydrogen pressure. At a critical hydrogen concentration the nucleation and growth of the β -phase is initiated, here large quantities of hydrogen can be dissolved in the metal by a slight increase in hydrogen pressure. For the reason of a nearly flat pressure plateau, the corresponding pressure is called the plateau pressure. The hydrogen pressure increases steeply with hydrogen concentration, after the α -phase is completely transformed to the β -phase. The width of the plateau is a measure of the miscibility of the two phases, which shrinks for higher temperatures and eventually disappears at the critical temperature.

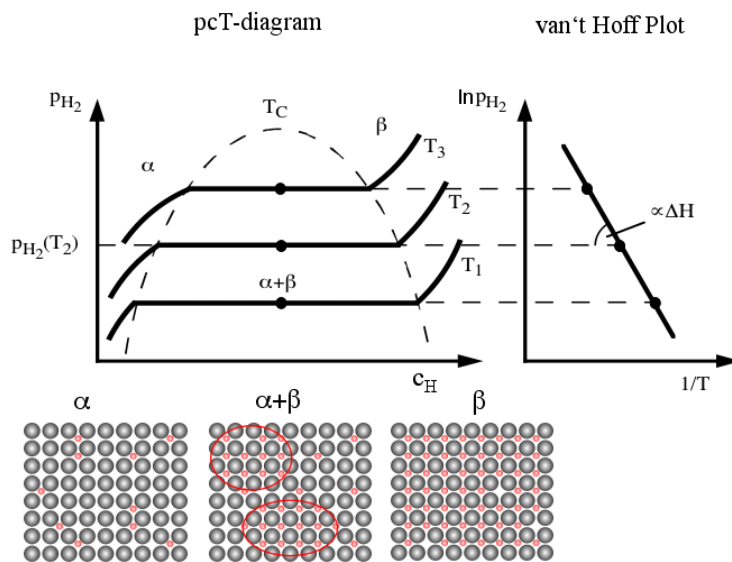


Figure 2: A pressure-composition isotherm for hydrogen absorption where the three states are shown below. A characteristic flat plateau pressure is formed for intermediate hydrogen concentration. The corresponding Van 't Hoff plot is shown on the right [28].

During the transition from a metal to a metal hydride three phases are present at the coexistence region: the hydrogen gas, the solid solution and the metal hydride. For thermodynamic equilibrium the chemical potential of the three phases must be equal:

$$\mu_{gas}(P, T) = \mu_{\alpha}(P, T, c_{\alpha}) = \mu_{\beta}(P, T, c_{\beta}) \quad (2)$$

Following Gibb's phase rule $F = C - P + 2$, with F the number of independent state variables, C the number of components and P the number of different phases, one variable is sufficient to describe equilibrium. Therefore all variables (P, T, c) are coupled, such that for a given temperature all other variables are fixed. Now the chemical potential, or Gibbs free energy, can be described with only one parameter:

$$\Delta G = RT \ln \left(\frac{p(T)}{p_0} \right) \quad (3)$$

Where R is the gas constant, T is the temperature, $p(T)$ is the plateau pressure and $p_0 = 1 \text{ atm} = 1.013 \text{ bar}$. This equation yields the Van 't Hoff equation:

$$\ln \left(\frac{p(T)}{p_0} \right) = \frac{\Delta G}{RT} = \frac{\Delta H}{RT} - \frac{\Delta S}{R} \quad (4)$$

Hence, a plot of $\ln \left(\frac{p(T)}{p_0} \right)$ against $\frac{1}{T}$ yields a straight line such that the formation enthalpy can be extracted from the slope and the formation entropy from the intersection with the y-axis. As the entropy change is dominated by the change from gaseous hydrogen to dissolved hydrogen, it equals approximately $-130 \text{ J K}^{-1} \text{ mol}^{-1}$ for all metal hydrides. Therefore, the main characteristic parameter of a metal hydride system is the enthalpy term. The formation enthalpy varies widely for metal hydrides, and describes the stability of the M-H bond [29], [30].

The absorption or desorption of hydrogen can be understood from the PCI and the Van 't Hoff equation. There is a thermodynamic driving force for hydrogen absorption when the hydrogen gas pressure is higher than the equilibrium pressure, as in this case the Gibbs free energy is negative for the hydrogenation reaction. Evidently, hydrogen will desorb from the metal hydride by either increasing the temperature or decreasing the hydrogen gas pressure as this inverts the sign of the Gibbs free energy. It is important from an application point of view that the M-H bond is sufficiently strong in order to guarantee safe and reliable storage; on the other hand the M-H bond should be weak enough to release the hydrogen relatively easily. As the formation enthalpy determines the amount of energy necessary to release the hydrogen from the metal hydride, this parameter characterises the stability of a metal hydride. Typically the Van 't Hoff equation is used to set a target for the formation enthalpy of a metal hydride suitable for hydrogen storage applications. The desired operating range of metal hydrides is between $100 \text{ }^\circ\text{C}$ and $150 \text{ }^\circ\text{C}$, and 1 and 100 bar e.g. for desorption of hydrogen to occur at 1 bar H_2 and $100 \text{ }^\circ\text{C}$, the formation enthalpy has to be $\Delta H = -49 \text{ kJ mol}^{-1}$.

The formation enthalpy for β -magnesium hydride (MgH_2) is larger ($\Delta H = -75 \text{ kJ mol}^{-1}$) than the desired value, originating from the ionic nature of the Mg-H bond. Consequently the equilibrium pressure at standard conditions is low, and a high temperature ($280 \text{ }^\circ\text{C}$ at 1 bar H_2) is required for hydrogen desorption. In principle, hydrogen absorption should occur at room temperature according to thermodynamics, however in general hydrogen sorption is limited by the kinetics of the reaction [14], [29].

The chemical reaction of magnesium with molecular hydrogen consists of the following sequence of steps [29], [31]:

1. Physisorption of molecular hydrogen
2. Dissociation of molecular hydrogen and chemisorption of atomic hydrogen
3. Diffusion into the subsurface and bulk lattice sites
4. Hydride formation by nucleation and growth

There is an asymmetry in diffusion as hydrogen diffuses through a metal hydride during absorption, whereas diffusion occurs through metal for hydrogen desorption [32]. The primary limiting steps for magnesium are: dissociation of hydrogen on the surface or surface passivation layer and diffusion of hydrogen through surface oxides and magnesium hydride [29], [33]. A pure magnesium surface exhibits a high activation energy for molecular hydrogen dissociation, such that catalysts (typically Pd, Fe, Ni, V, Zr and Ti) are often used to enhance the dissociation rate [34]. Remarkably, not the entire surface needs to be coated by a catalyst to improve the dissociation rate. A sparse distribution of small catalyst particles is sufficient to “flood” the surface with hydrogen atoms [35].

As magnesium is an alkaline earth metal it readily forms a surface magnesium oxide (MgO) in virtually any oxygen atmosphere, even in an UHV environment [12]. In general the oxide surface is difficult to penetrate for hydrogen, thus limiting the surface penetration rate. An activation step is usually necessary to circumvent the problems due to the surface oxide. The activation procedure typically consists of high-temperature (400 °C) heating cycles in a hydrogen atmosphere or in vacuum, which is believed to break the oxide surface layer, such that the bare metal surface is exposed [35]. After exposure of the metal to air, the activation step must be repeated. A proper catalyst can eliminate the need for an activation step even after long-term exposure to air, as the catalyst supplies large quantities of hydrogen atoms such that the blocking effect of the oxide is diminished [36].

In the first stages of the formation of the β -phase, the local hydrogen concentration is the highest in the surface region which leads to faster nucleation and growth of the metal hydride at the surface region. The oxide surface layer acts as a heterogeneous nucleation site for the β -phase, which increases the nucleation rate compared to the oxide free case. Hence, many nucleation sites of the β -phase are located at the Mg surface or, if oxidized, at the Mg-MgO interface region, eventually leading to the coalescence of the local hydride grains to form a continuous hydride layer [34]. As the diffusion activation energy of MgH_2 is higher than pure Mg, the hydride surface layer is an additional diffusion barrier. At this stage the limiting factor for complete hydrogenation is the growth of the β -phase caused by the slow diffusion of hydrogen atoms through the β -phase and in general limit the total hydrogen capacity [31]. For bulk magnesium a hydride surface layer of 30-50 μm completely blocks further hydrogen absorption [14], [32]. Yet, in nanostructured magnesium the blocking effect due to the poor diffusion in MgH_2 is negligible as the typical length scale is below the diffusion length.

2.2 High pressure magnetron sputtering

Sputtering is a process of bombarding a target material with energetic ions that leads to the ejection, or sputtering, of the surface atoms. Typically, an inert gas (Ar or Kr) is used as a source for the ions which are generated by discharge. The positively charged ions are accelerated by the local electric field. Along the trajectory more atoms are ionized due to ion-atom collisions. These ions bombard the target surface at which the key processes are the sputtering of surface atoms and the production of secondary electrons. Sputtered atoms move away from the target and (in a system like the nanocluster source) are assisted by the gas flow towards the sample chamber. Secondary electrons are confined by the magnetic field of the magnetron head, such that locally the electron density and total path length are significantly increased. The secondary electrons have sufficient energy to ionize inert gas atoms, therefore the ionization probability is effectively enhanced leading to a dense plasma of ions near the magnetron head [37]–[39].

The efficiency of sputtering is called the sputtering yield S and is defined as the number of sputtered atoms per incident ion. Sputtering yield is a parameter that is mainly affected by the target material, sputter gas, accelerating voltage and gas pressure. A simplistic model of sputtering with ion energies smaller than 1 keV results in the following description of the sputtering yield [40]:

$$S = \frac{3\alpha}{4\pi^2} \frac{4m_i m_t}{(m_i + m_t)^2} \frac{E}{U_0} \quad (5)$$

Where U_0 is the surface binding energy of the target material, E the energy of the incident ion, α a monotonic function of E and m_i and m_t are the masses of the ion and target atom, respectively. The term in the middle arises from the assumption of a pure elastic collision between the ion and target atom. Although being an approximation, it shows the general features of a sputtering process. As intuitively expected, sputtering yield decreases for stronger bound materials and increases by increasing the ion energy. This implies that a sectioned target (consisting of two or more elements) has different sputter yields for every element. Hence, the vapour composition is coupled to the target composition via the sputter yield.

2.2.1 Inert gas condensation: Nucleation and growth

Combining the high inert gas pressure and the enhanced degree of ionization by virtue of the magnetron, this leads to a high density of sputtered atoms. Supersaturation of the sputtered vapour is achieved which results in a thermodynamic driving force for solidification. Classical nucleation theory can be used to describe and understand the thermodynamics in an intuitive way by means of homogeneous and heterogeneous nucleation. Homogeneous nucleation occurs when there is a thermodynamic driving force for solidification and no impurities are present i.e. the system must be of high purity. Whereas heterogeneous nucleation requires the presence of impurities to occur. Nucleation of a spherical solid phase in the vapour phase results in volume (ΔG_V) and interface (γ) contributions to the Gibbs free energy of the system:

$$\Delta G(r) = 4\pi r^2 \gamma - \frac{4}{3} \pi r^3 \Delta G_V \quad (6)$$

Hence, the system's free energy is reduced by solidification at the cost of an increase due to interface energy. Nucleation of small nuclei therefore always increases the free energy, where a positive maximum is achieved at the critical radius:

$$r^* = \frac{2\gamma}{\Delta G_V} \quad (7)$$

Nuclei have to outgrow the critical radius in order to become thermodynamically stable. Therefore, in order to achieve a stable solid nucleus, a free energy barrier must be overcome, given by:

$$\Delta G(r^*) = \frac{16\pi\gamma^3}{3\Delta G_V^2} \quad (8)$$

All nuclei with a radius smaller than the critical radius are predicted to evaporate due to their thermodynamic instability. Nuclei are formed at a rate that is proportional to the Boltzmann factor of their free energy $\Delta G(r)$ i.e. $e^{-\frac{\Delta G(r)}{kT}}$. Hence, due to the thermal fluctuations the free energy barrier can be overcome. Nucleation on a surface causes the exposed surface of the solid phase to decrease, which results in a decreased surface term in the free energy equation. Therefore, the overall free energy $\Delta G(r)$ is reduced for heterogeneous nucleation leading to a higher nucleation rate. As the nuclei exceed the critical radius further growth involves several processes in parallel. The main processes are the net attachment (accompanied with evaporation) of single atoms to the surface (accretion) and merging after a collision (coalescence) [41]. Nucleation of multiple elements is a rather complex system, as individual material properties has to be taken into account (melting temperature, surface energy) but aside of that also the interaction between the elements affects the nucleation e.g. formation of an intermetallic. Yet, for a sputtering system such the nanocluster source (explained in the following section) the nucleation and growth is fairly well understood [15], [16], [42].

3. Experimental procedures

3.1 Nanoparticle cluster source

Nanoparticles are produced with a home-modified Nanogen 50[®] nanocluster source manufactured by Mantis LTD[©] (Figure 3). The system consists of two chambers: the aggregation chamber and the sample chamber. Inside the aggregation chamber a target material (cathode) is placed on top of a water cooled magnetron head. The target material is enclosed by a cap which also serves as an anode, such that a potential difference can be applied between the target and the anode cap. A gas inlet is positioned behind the magnetron head, resulting in a gas flow over the target. Typically the gas is an inert element such as Argon (Ar), which is used in the synthesis of Mg-Ti nanoparticles.

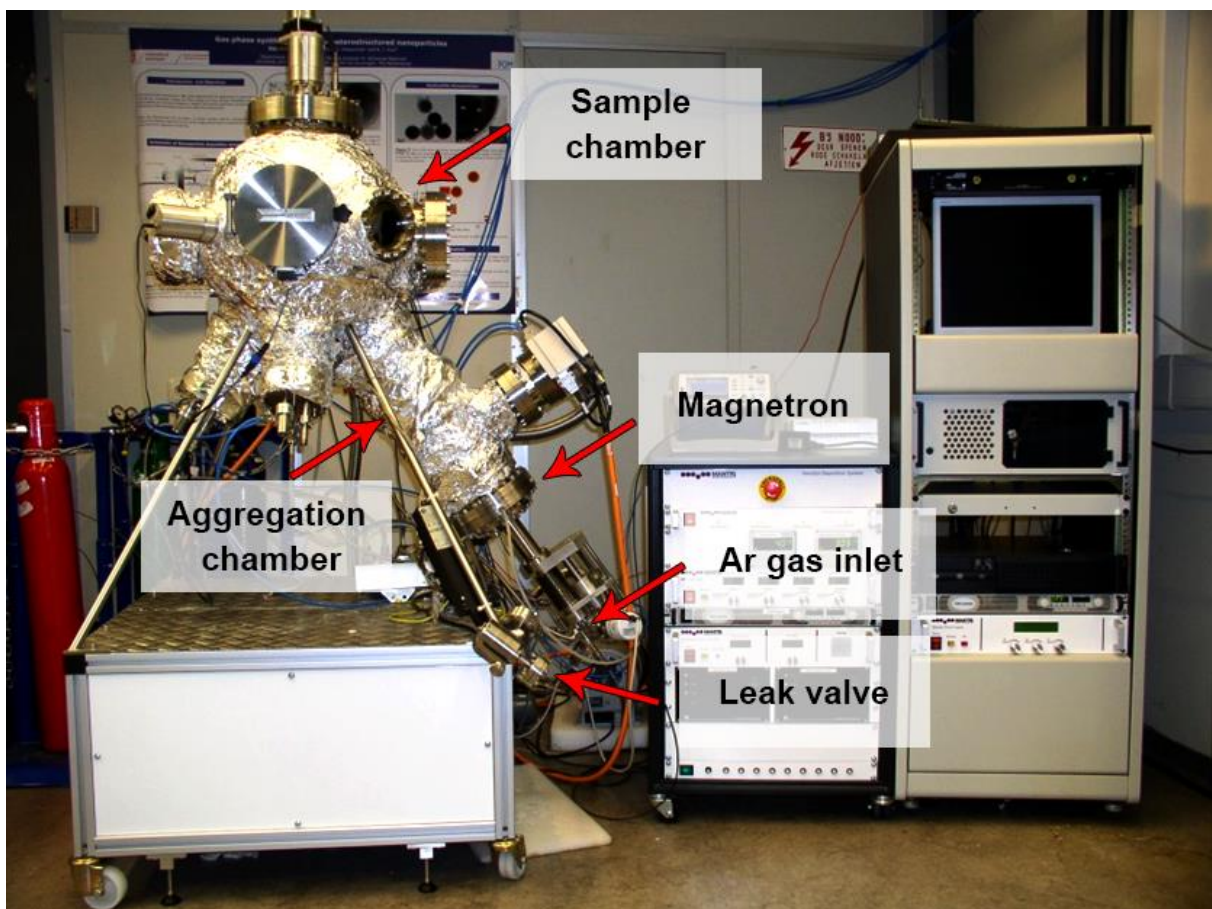


Figure 3: The home-modified Nanogen 50 nanocluster source.

The aggregation chamber and the sample chamber are separated by a 3.8 mm aperture, which causes a pressure difference of several orders of magnitudes when the system is evacuated to high vacuum. After evacuation the pressure in the sample and aggregation chamber is 10^{-8} mbar and 10^{-6} mbar, respectively. As Ar is introduced, the respective pressures increase to 10^{-4} mbar and 10^{-1} mbar. Besides forming and sustaining a plasma near the magnetron head, Ar also fulfils the role of cooling and drift gas. Energy and momentum is transferred from the sputtered atoms to the inert Ar gas during elastic collisions, such that only close to the magnetron head the sputtered atoms are still in their high energy state. As nucleation occurs the nanoparticles grow and are transported and cooled by the Ar gas. Hence, the Ar gas directly impacts the thermal environment in which the nanoparticles

can grow. An additional gas (CH_4 or H_2 in this thesis) can be introduced via a high precision leak valve which assists nanoparticle nucleation. Due to the compact design of the cluster source, the parameters that affect the plasma generation and cluster nucleation and growth conditions are highly coupled. The most important control features are the Ar gas pressure and the ion current. Previous work has shown that these parameters affect the thermal environment that allows reasonable good control over the nanoparticle's nucleation and growth conditions [15], [16].

3.2 Hydrogenation experimental setup

The TEM samples were hydrogenated in a home-made sample holder, which can hold up to nine TEM substrates simultaneously (Figure 4). Before hydrogenation the system is pumped down to 10^{-2} mbar, and flushed several times with molecular hydrogen gas to minimize contamination. The sample holder is heated by a PID controlled oven to the required temperature. For all hydrogenation experiments, the hydrogen gas pressure was set to 10 bar and the temperature set to 250 °C, unless specified otherwise.

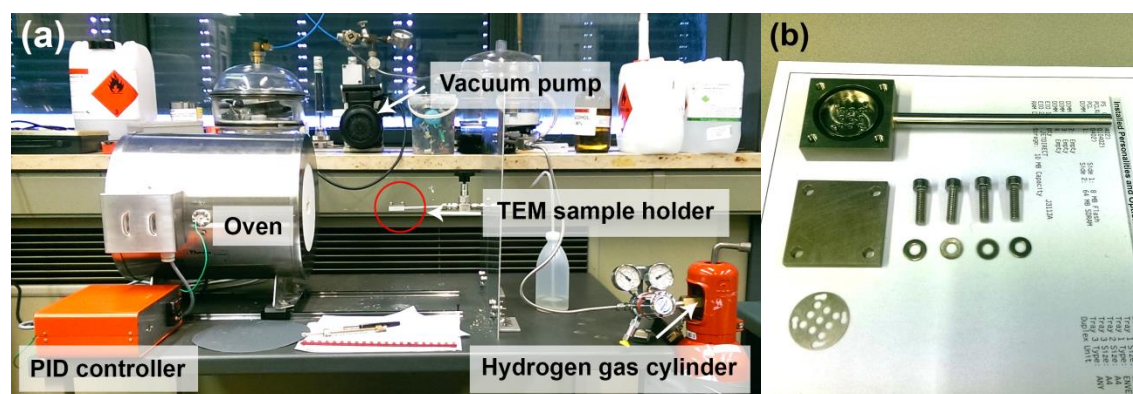


Figure 4: (a) The hydrogenation experimental setup in and (b) the sample holder for hydrogenation of TEM samples.

3.3 TEM characterization with JEOL 2010 and JEOL 2010F

A JEOL 2010 TEM with a LaB_6 electron source operating at 200 kV has been used to characterize the nanoparticles by means of bright field imaging and electron diffraction. Furthermore, the TEM is equipped with an Energy Dispersive X-ray (EDX) spectrometer to measure the chemical composition of the nanoparticles. For High Resolution TEM (HRTEM) imaging a JEOL 2010F with a Field Emission Gun (FEG) electron source has been used. The enhanced coherence and brightness of the FEG result in a better performance in terms of spatial resolution (information limit) compared to a LaB_6 electron source.

Image formation in a TEM is similar to a common visible-light microscope i.e. by diffraction of waves. Compared to visible light a much smaller wavelength is obtained by accelerating electrons to 200 kV, which results in a higher spatial resolution according to the Rayleigh criterion. The accelerated electrons move, before reaching the sample and after being transmitted through the sample, through typically two apertures and several (e.g. seven) magnetic lenses to end up on the phosphor screen or the CCD camera. Due to the imperfections of magnetic lenses the resolution of the TEM is not diffraction limited as given by the Rayleigh criterion, but rather by chromatic and in particular spherical aberrations of the lenses.

From a more abstract and quantitative point of view these effects are incorporated in the so called transfer function, which is of particular relevance for high resolution TEM imaging that is part of phase-contrast imaging. In this case we thus consider the phase-contrast transfer function. It describes how the microscope transfers the locally varying (in x,y plane) phase differences coming out of the sample into the image (when the electron beam progresses in the z-direction). More precisely, it relates the intensity of the image to the exit wave coming out of the specimen. Since the transfer function acts as a convolution in real space, it is very convenient to consider the process in reciprocal space, where the effect of the transfer function simply becomes a multiplication. Therefore, the transfer function is a function of spatial frequency (reciprocal distances) and apart from describing the image contrast it also includes a description of the resolution of the microscope. For high resolution imaging high spatial frequencies are required in the image, but due to the spherical aberrations the resolution is limited. This is clear from the oscillatory behaviour of the transfer function that originates from the interplay of spherical aberrations and (de)focus. For low spatial frequencies the transfer function has a relatively constant value close to a phase shift of $-\pi/2$ (see Figure 5) such that these frequencies not only appear in the image with nearly constant phase, but more importantly that weak phase shifts (imaginary part) which are normally invisible, are transferred to amplitude contrast (real part) and thus directly affect image intensity. At higher spatial frequencies the transfer function crosses zero and starts oscillating as shown in Figure 5. In this frequency range image interpretation is not straightforward as the contrast in the image is heavily dependent on the spatial frequency e.g. in HRTEM the atoms appear both black and white. Therefore, the first crossover point in case of optimum defocus (i.e. where the first passband has the largest frequency range with values at least 70% of plus or minus $\pi/2$) is defined as the point resolution limit i.e. information below this spatial frequency the image can be more intuitively interpreted, yet higher resolution is present in the image. Due to the interplay of the spherical aberration and defocus, the resolution can be optimized by slightly under-focusing the specimen, which is related to the so-called Scherzer defocus. Chromatic aberrations, incoherence of the electron source, temporal variations in source voltage and in lens current and voltage further modulate the transfer function such that high spatial frequency information is damped. This envelope function limits high spatial frequencies which is called the information limit, beyond this point no frequencies containing relevant information are transmitted in the image regardless of the focus setting. Hence, the point resolution and information limit are the figures of merit to describe the performance of a TEM [43].

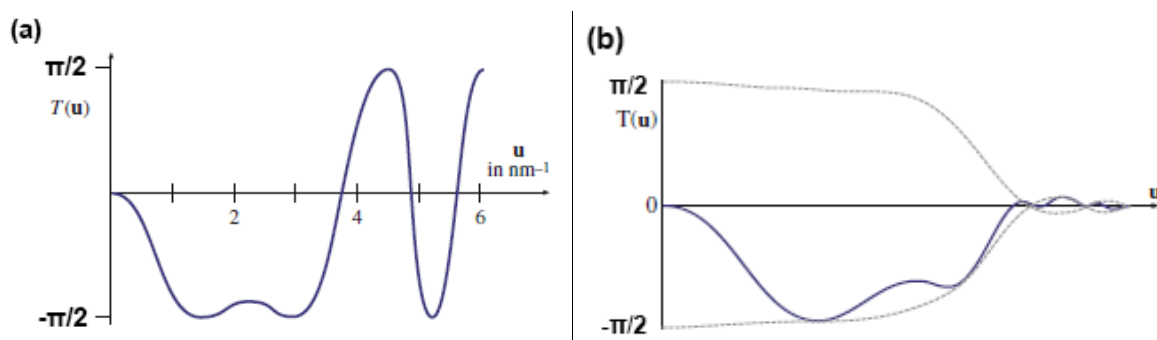


Figure 5: The phase-contrast transfer function (a) without the damping envelope function (b) and modulated by the envelope function.

This description directly gives insight in the formation of bright field and selected area electron diffraction (SAED) pattern as shown in Figure 6. When a parallel beam is incident on the specimen a diffraction pattern forms in the back focal plane (BFP) and are further focused into an image on the phosphor screen or CCD camera. At the BFP the high angle diffracted electrons are filtered by inserting an objective aperture which yields enhanced diffraction contrast. This comes at the cost of the resolution as high spatial frequency information is not transmitted to the image. With the JEOL 2010 no HRTEM images can be readily achieved (although its point resolution is 0.23 nm) such that the limited resolution is not an issue. In diffraction mode the objective lens strength changes such that the SAED pattern is focused on the phosphor screen or CCD camera. A SAED pattern can be obtained from a specific location in the specimen by inserting a selected area aperture in the image plane.

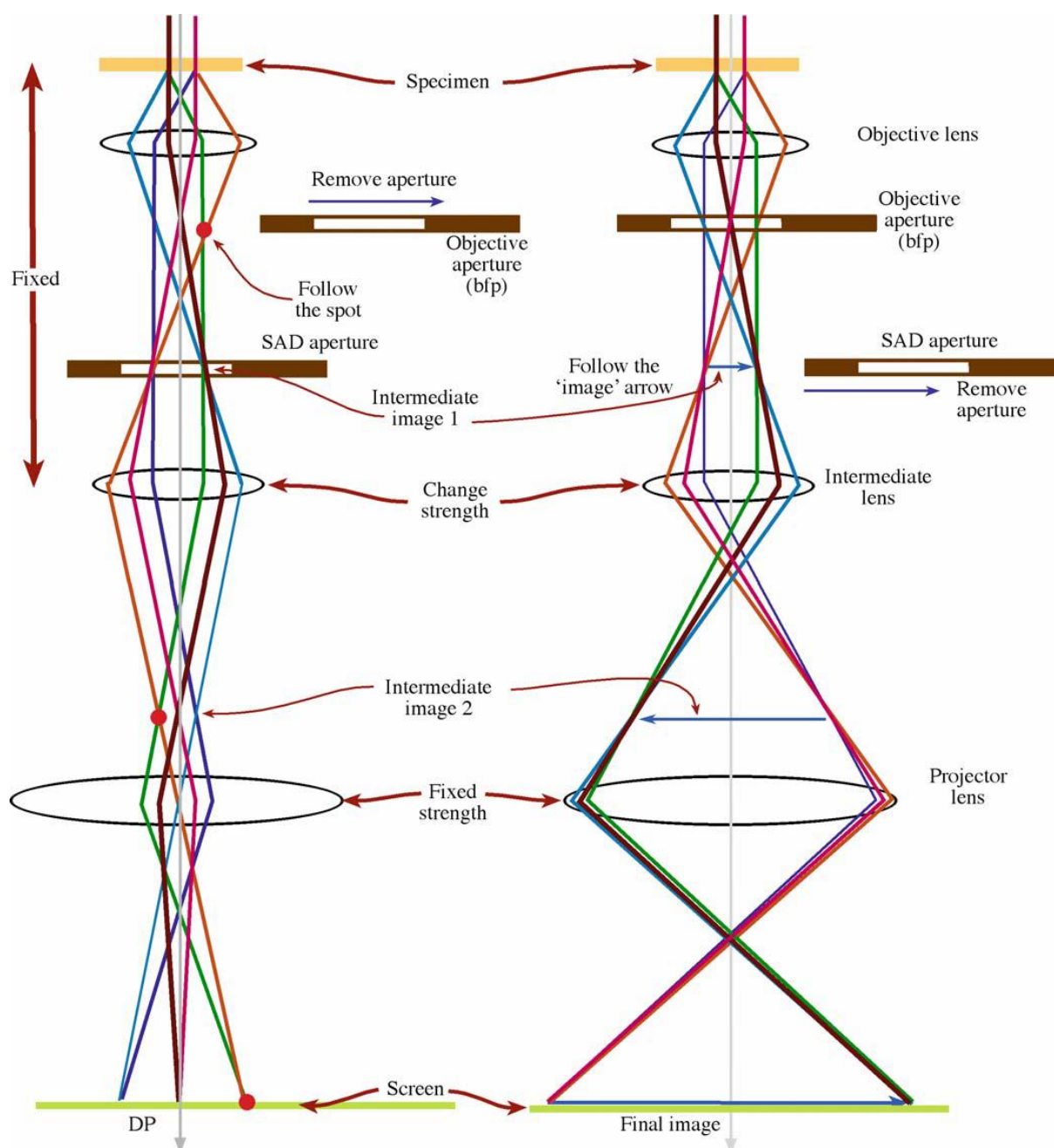


Figure 6: Basic operations of a TEM (Left) Diffraction mode (Right) image mode [43].

4. Results and discussion

4.1 Nucleation rate control of Mg-Ti nanoparticles stimulated by CH₄ and H₂ gas

High pressure magnetron sputtering has been utilized to synthesize Mg-Ti nanoparticles in the gas phase by using a sectioned target consisting of Mg and Ti. Despite achieving supersaturated Mg and Ti vapour by virtue of the high pressure operating regime of the magnetron, a sufficiently high and stable homogeneous nucleation rate of Mg-Ti nanoparticles could not be reached. This is demonstrated in Figure 7, where the measurement of a Quartz Crystal Microbalance (QCM) during a deposition is shown as a function of time. Initially the measured mass flux is constant and a sudden decrease in mass flux occurs after approximately 15 minutes followed by a gradually decaying slope that approaches zero. Figure A1 in the Appendix shows that the particle size remains fairly constant, but the surface coverage (fraction of covered surface) decreases substantially. Hence, a decreasing nucleation rate is the dominant process that limits stable and constant nucleation rate during sputtering.

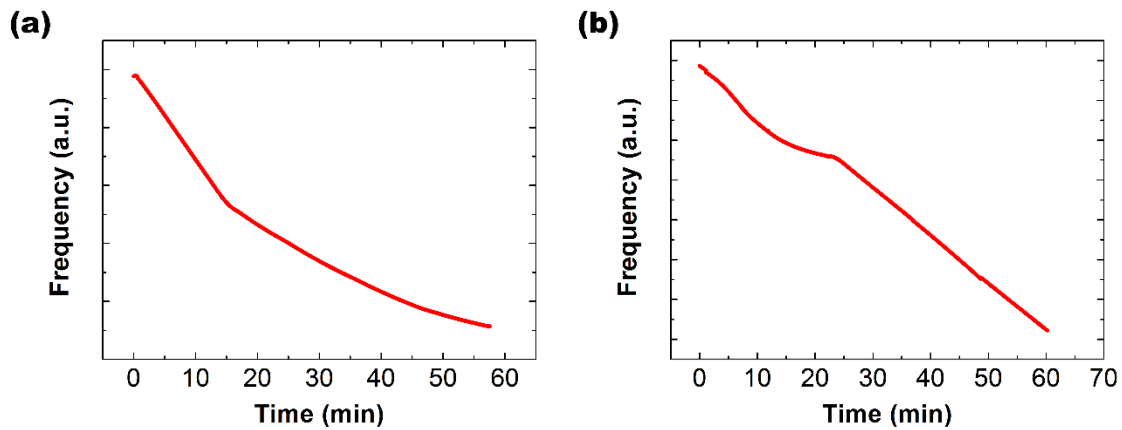


Figure 7: QCM frequency as a function of sputtering time. (a) After 15 minutes of sputtering a sudden change in mass flux is observed, indicating a change in nucleation and growth conditions. (b) After 20 minutes of sputtering the mass flux decays to zero. When methane is introduced the mass flux becomes stable for the remaining deposition time.

The initial stable nucleation rate is understood on the basis of heterogeneous nucleation. As the sputter target is stored in air a thin surface passivation layer is formed e.g. MgO and TiO₂. Hence, initially, the sputtered atoms contain a fraction of impurities which allow heterogeneous nucleation in the gas phase of Mg and Ti. Over time the passivating surface layer is reducing in size as a torus-like erosion profile is developed that eventually completely penetrates the surface passivation layer. This effect results in a quickly decaying impurity concentration that acts as a heterogeneous nucleation site, such that the nucleation rate decreases. When virtually no impurities are added to the plasma, nucleation relies only on homogeneous nucleation of Mg and Ti. During all depositions a stable homogeneous nucleation rate could not be achieved. A higher and more stable nucleation rate is achieved by introducing a continuous flow of methane or hydrogen gas to the aggregation chamber. The nucleation rate is found to be exceptionally stable over a large time span (at least over 30 minutes) when the pressure of methane or hydrogen is approximately 10⁻⁴ mbar in the aggregation chamber compared to the Ar pressure at 10⁻¹ mbar.

4.2 Nucleation and growth of Mg-Ti nanoparticles: The effect of the gas environment

4.2.1 Synthesis in an Ar gas environment

Mg-Ti nanoparticles that are synthesized in a pure Ar gas environment have a diameter of approximately 40 nm and a hexagonal shape in projection (Figure 8a). Frequently, nanoparticles are grown which possess a small (1-3 nm) core and the core is slightly bigger (7-12 nm) for other depositions under identical conditions. Hence, even though the nucleation rate is stable for several minutes when the target is oxidized, it is typically difficult to reproduce particles with similar characteristic features when only Ar is used as sputter gas. For instance, the structural motif of the nanoparticles cannot be reproduced as illustrated in the Appendix in Figure A2. As will be shown in the next sections the reproducibility is greatly improved when adding a slight amount of methane or hydrogen to the Ar sputtering gas.

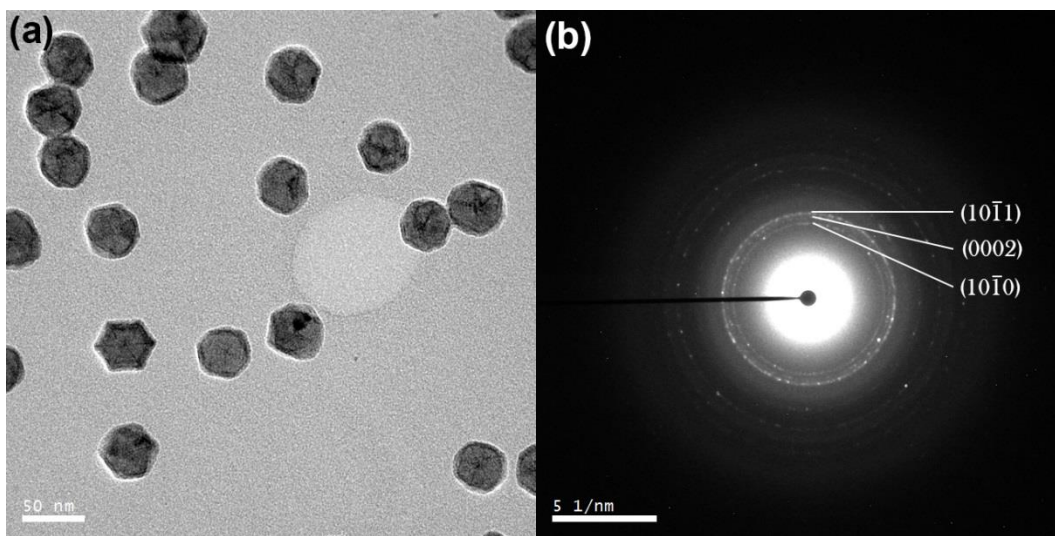


Figure 8: (a) Bright field TEM image of $\text{Mg}_{88}\text{Ti}_{12}$ nanoparticles grown in an Ar gas environment (b) and its corresponding SAED pattern.

Selected area electron diffraction (SAED) has been used to investigate the crystal structure of the nanoparticles. The nanoparticles have a composition of 88 ± 1 at% Mg and 12 ± 1 at% Ti as measured by EDX and have a hexagonal closed packed (HCP) crystal structure as the low index $\{10\bar{1}0\}$, $\{0002\}$ and $\{10\bar{1}1\}$ planes are resolved in the SAED pattern, as shown in Figure 8b. The lattice parameters of the HCP lattice are $a = 3.22 \pm 0.03 \text{ \AA}$ and $c = 5.16 \pm 0.05 \text{ \AA}$, which compares well with the crystal structure and lattice parameters of pure Mg. Besides the sharp HCP rings, two broad rings are observable which are attributed to the $\{200\}$ and $\{220\}$ planes of MgO. The broad MgO rings stem from the thin shell that is visible around the nanoparticle at higher magnification. The MgO shell is confirmed by single nanoparticle SAED pattern as shown in Figure 9, where the Mg $\{10\bar{1}0\}$ and MgO $\{2\bar{2}0\}$ planes are resolved. The streaking of the MgO $\{2\bar{2}0\}$ plane in the $[220]$ direction originates from the small thickness of the MgO shell in the $[220]$ direction. An orientation relation (OR) follows from the SAED pattern i.e. MgO $\{2\bar{2}0\}$ planes are parallel to Mg $\{10\bar{1}0\}$ planes. Hence, the OR is given by $\text{Mg}[0001]//\text{MgO}[001]$ and $\text{Mg}\{10\bar{1}0\}//\text{MgO}\{220\}$. The OR is further supported by HRTEM images of the Mg-Ti nanoparticle along the Mg $[0001]$ axis, such that the orthogonal MgO (200) and (020) planes are resolved, as shown in Figure 10a. Based on previous results for pure Mg nanoparticles [12], it is expected that the hexagonal shape in projection originates from six Mg $\{10\bar{1}0\}$ facets, but

since they are covered with a thin MgO shell, actually MgO{220} planes form the outer facets. This is remarkable since for MgO the surface energy of the {200} facets is much lower than of the {220} ones. This shows that the MgO orientation is governed by the underlying Mg and not by the free surface. Moreover, it has been observed that the (smooth) MgO (220) surface under the influence of the electron beam of the TEM can reconstruct in alternating MgO (200) and MgO (020) facets and thus a jagged surface, increasing the surface area by about a square-root of two, but still decreasing surface energy.

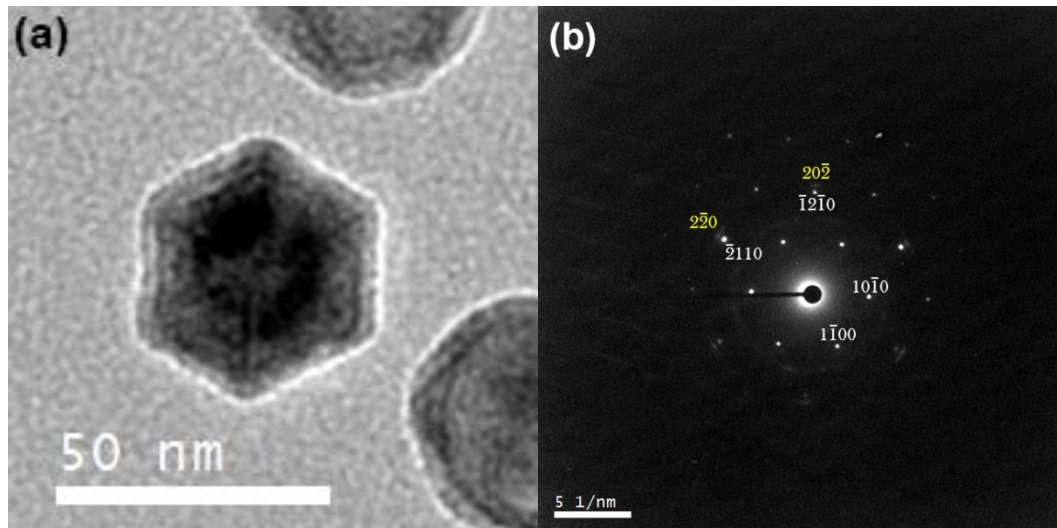


Figure 9: (a) Bright field high magnification TEM image of an Mg₈₈Ti₁₂ nanoparticle (b) and its corresponding SAED pattern viewed along the [0001] axis of Mg. The HCP Mg-Ti and FCC MgO planes are indexed in white and yellow, respectively.

Remarkably, no HCP Ti could be identified in the SAED pattern. Combined with the structural motif, this suggests that the Ti is distributed over the Mg lattice forming a solid solution of Mg-Ti. The projection of the nanoparticle along the Mg [0001] axis indicates that the nanoparticle is faceted by the $\{10\bar{1}i\}$ planes, where i is an integer i.e. the prismatic or pyramidal planes. Furthermore, the particles are often viewed along the Mg [0001] direction which suggests the nanoparticles are faceted by $\{0002\}$ planes as well. A series of bright field TEM images over a large tilt angle range (-65 to +65 degrees) are 3D reconstructed (tomography) to obtain a 3D visualization of the nanoparticle shape, as shown in Figure 11. The nanoparticle shape very well resembles a truncated hexagonal pyramid where the facets consist mainly of $\{10\bar{1}1\}$ and $\{0002\}$ planes. Indeed, HRTEM bright field viewing along a direction orthogonal to the [0001] direction (Figure 10b) shows that the (0002) plane is parallel to a facet. More noticeably, viewing along this direction confirms that the side facets are not parallel to the Mg $\{10\bar{1}0\}$ planes as was observed for pure Mg nanoparticles [12], but rather Mg $\{10\bar{1}1\}$ planes.

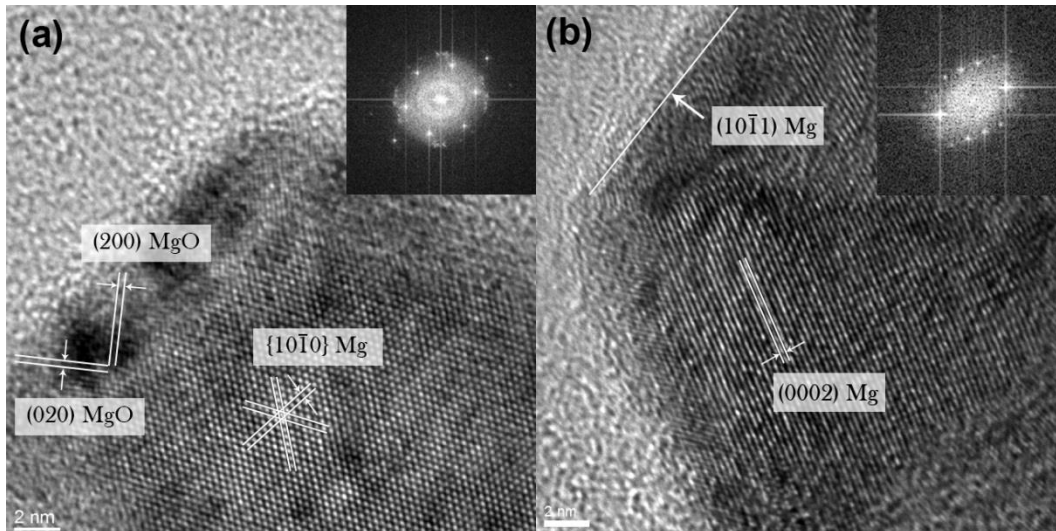


Figure 10: HRTEM bright field images of $\text{Mg}_{88}\text{Ti}_{12}$ nanoparticles (a) along the $[0001]$ zone axis that shows the OR between Mg and MgO (b) along the $[11\bar{2}0]$ axis orthogonal to the $[0001]$ axis where the $\{0002\}$ and $\{10\bar{1}1\}$ planes are parallel to a facet. The FFTs are shown in the insets.

A typical feature of the alloyed nanoparticles is observed in high magnification TEM bright field images. Viewing along the $[0001]$ direction, which yields a hexagonal nanoparticle in projection, shows darker contrast pointing radially outward from the 1-3 nm core along the $[11\bar{2}0]$ directions to the six vertices. The contrast of this phenomenon depends on the orientation of the nanoparticle i.e. the six-fold symmetry is not always visible. Possibly the contrast is composed due to crystal twinning or to a partial phase segregation of Ti to this unique structure. This latter phenomenon could then originate from the difference in nanoparticle structure for Mg-Ti alloyed and pure Mg nanoparticles as was already mentioned above and is discussed in more detail below. However, a clear understanding of the origin of this phenomenon is unfortunately still missing.

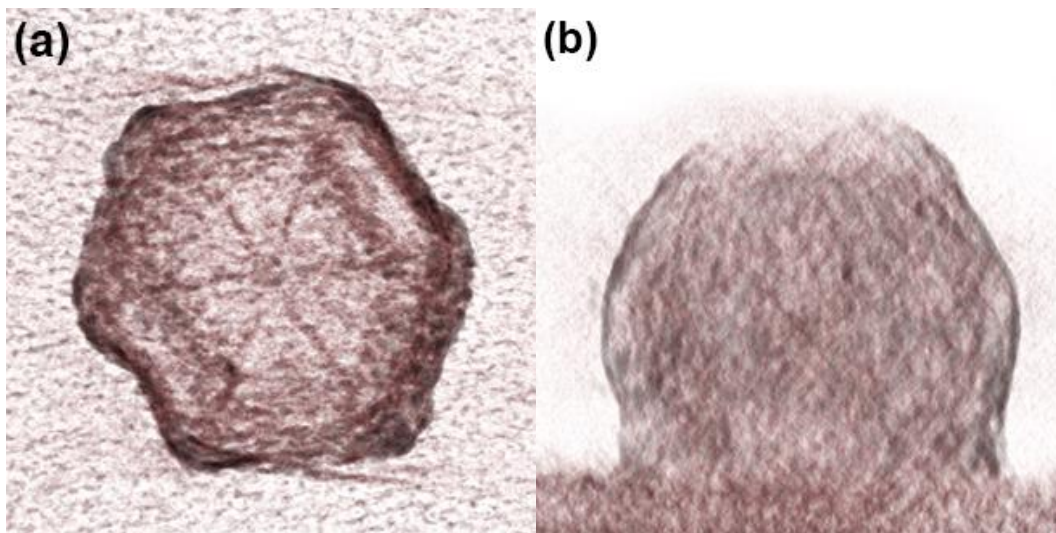


Figure 11: 3D reconstruction of the particle shown in Figure 9 (a) shown from the top (b) and shown normal to a facet.

The nanoparticle is thus faceted by $\{10\bar{1}1\}$ and $\{0002\}$ planes which is unlike pure Mg nanoparticles which form facets parallel to the $\{10\bar{1}0\}$ and $\{0002\}$ planes [12]. The shape of nanoparticles is determined by the thermodynamics and kinetics of the nucleation and growth conditions.

Thermodynamics determine the equilibrium shape of a particle based on surface energy, however the kinetics of growth can alter the final shape by affecting growth rates of specific crystal planes [44]. Assuming thermodynamic controlled growth such that the shape is predominantly governed by the surface energy, the different shape of Mg-Ti nanoparticles compared to pure Mg nanoparticles can be understood based on the Wulff construction.

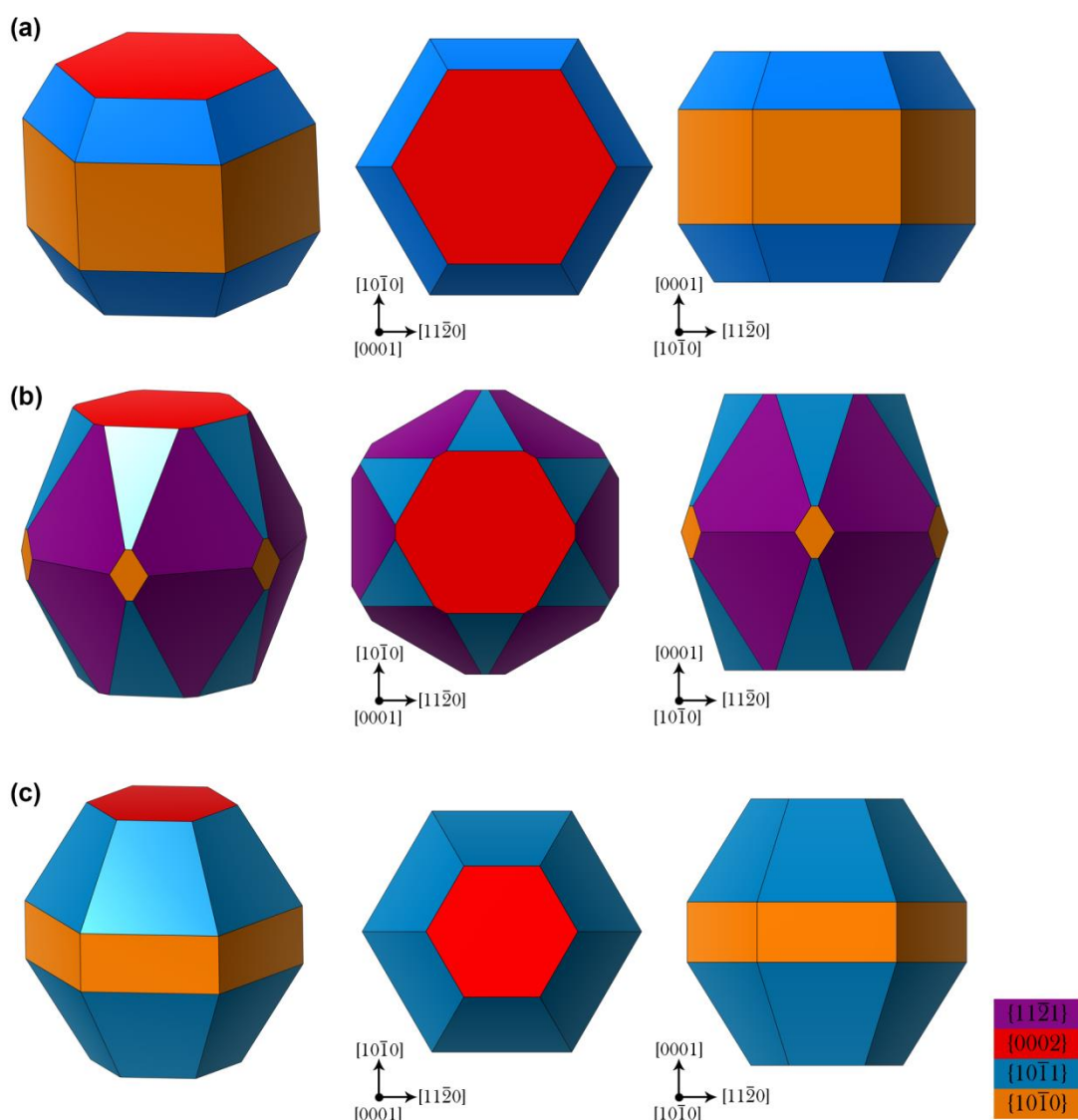


Figure 12: Equilibrium shapes based on the results of [45] for (a) pure Mg nanoparticles (b) pure Ti nanoparticles. (c) The nanoparticle's shape based on the 3D reconstruction and SAED patterns of the present work.

The thermodynamic equilibrium shape of pure Mg and Ti crystals has been predicted by applying the Wulff construction based on DFT calculated surface energies. The fractional contribution of the predicted surfaces have been estimated as 38% $\{10\bar{1}1\}$, 37.8% $\{10\bar{1}0\}$ and 24.2% $\{0001\}$ planes for Mg, whereas Ti consist of 55.5% $\{11\bar{2}1\}$, 24.5% $\{10\bar{1}1\}$, 17.2% $\{0001\}$ and 2.8% $\{10\bar{1}0\}$ planes [45]. The resulting shapes are shown in Figure 12; note that Mg is predicted to be faceted as a hexagonal prism, while Ti is predicted to form a hexagonal pyramid in both cases the surface energy is reduced by truncating the vertices. The former prediction corresponds well with previous observations of Mg nanoparticles, while the combination of the two is similar to what is observed for Mg-Ti nanoparticles. This implies that a slight amount of Ti could be present in the particle as a solid

solution such that surface energy of particular crystal planes is affected. Therefore the alloyed structure increases the $\{10\bar{1}0\}$ surface energy, while decreasing the $\{10\bar{1}1\}$ surface energy. This results in a particle that is predominantly faceted by the $\{10\bar{1}1\}$ and $\{0002\}$ planes. Typically the lattice parameter of an Mg-Ti solid solution is reported to result in a compositional weighted linear combination of the respective lattice parameters of Mg and Ti. Yet, this effect is not observed in SAED patterns except for possibly a small contraction along the HCP c-axis. High resolution elemental mapping is required to further investigate the spatial dispersion of Ti and Mg in the nanoparticles.

The assumption of an alloyed structure is further assisted by combining EDX measurements with the structural motif. From EDX measurements the composition is measured to be Mg-rich at $88\pm 1\%$ Mg and $12\pm 1\%$ Ti. The resulting nanoparticles sometimes form a structural motif which consists of a small core (1-3 nm) and a large shell (~ 20 nm). If Mg and Ti would have phase segregated into a Ti core and an Mg shell, the Ti core would need to be significantly larger to account for the composition. As this is not observed in the bright field images it can be concluded that the Ti must be dispersed over the rest of the nanoparticle. Hence, all the characteristics of the nanoparticles indicate the formation of an alloyed structure for Mg and Ti that are according to thermodynamics immiscible in equilibrium in bulk.

4.2.2 Synthesis in an Ar-CH₄ gas environment

When methane is introduced during synthesis, the nanoparticle production is not only kept stable as a function of time but also the process becomes clearly more reproducible. Interestingly, the nanoparticles form a different structural motif (compared to the ones without methane addition) as is shown in Figure 13. A prominent core-shell structural motif is observed with a core diameter which is significantly larger than the core for the nanoparticles synthesized in a pure Ar environment. The nanoparticle consists of a 25 ± 3 nm core, surrounded by a 12 ± 3 nm shell which as a whole is enclosed in a 3-4 nm thin MgO outer shell, resulting in a narrow monodisperse size distribution of 56 ± 3 nm. The nanoparticles contain $85\pm 1\%$ Mg and $15\pm 1\%$ Ti as measured by EDX. The most frequently observed shape of the nanoparticles is hexagonal in projection similar to alloyed nanoparticles.

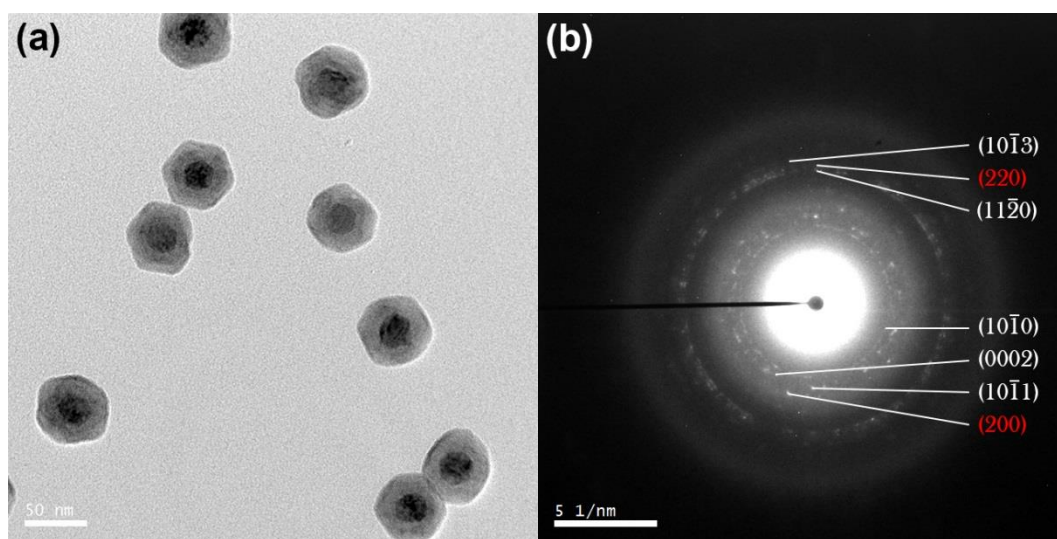


Figure 13: (a) Bright field TEM image of core-shell Mg₈₅Ti₁₅ nanoparticles grown in a methane gas environment and (b) its corresponding SAED pattern. The HCP Mg and FCC Ti planes are indexed in white and red, respectively.

From the SAED pattern HCP Mg is identified, since the low index $\{10\bar{1}0\}$, $\{0002\}$ and $\{10\bar{1}1\}$ planes are resolved. The lattice parameters of the HCP crystal structure are $a=3.22\pm 0.03$ Å and $c=5.20\pm 0.05$ Å, which compares well with pure Mg. In addition to the HCP Mg crystal structure another phase is present which is determined to have a cubic lattice with a face-centered cubic (FCC) symmetry as the $\{200\}$ and $\{220\}$ planes are visible. The lattice parameter of the FCC crystal structure is 4.40 ± 0.04 Å which matches with the crystal structure of TiC ($a=4.33$ Å).

Closer inspection of the core-shell nanoparticles reveals an OR between the core and the shell as deduced from a single nanoparticle SAED pattern as shown in Figure 14. Viewing along the $[0001]$ axis of Mg the $\{10\bar{1}0\}$ and $\{11\bar{2}0\}$ planes are visible. The TiC $\{220\}$ planes are also visible and are parallel to the Mg $\{11\bar{2}0\}$ planes, such that TiC is viewed along the $[111]$ axis. In projection, the Mg $\{10\bar{1}0\}$ planes are parallel to the nanoparticle facets and the TiC $\{220\}$ planes are parallel to the core-shell interface. Combined with the contrast of the bright field TEM image, this indicates that the nanoparticle has got a TiC core surrounded by an Mg shell. The presence of carbon in the core is further supported by high resolution EDX measurements of the core, although TiC may have a sub-stoichiometric composition. Therefore, the OR between the TiC core and Mg shell is given by Mg $[11\bar{2}0]$ //TiC $[220]$ and Mg $\{0002\}$ //TiC $\{111\}$ i.e. the HCP and FCC close-packed planes and close-packed directions are parallel. Identical to alloyed nanoparticles the core-shell nanoparticle is enclosed by a thin MgO shell, where the OR is given by Mg $[0001]$ //MgO $[001]$ and Mg $\{10\bar{1}0\}$ //MgO $\{220\}$. The shape of the nanoparticles appears to be identical to the alloyed nanoparticles, as SAED patterns of particles in various orientations (Appendix Figure A3 and A4) yield the result that the particle is faceted by the $\{10\bar{1}1\}$ and $\{0002\}$ planes. Despite forming a TiC core the effect of Ti on the surface energies of the shell cannot be neglected, which indicates that at least a slight amount of Ti is present in the subshell of the nanoparticle.

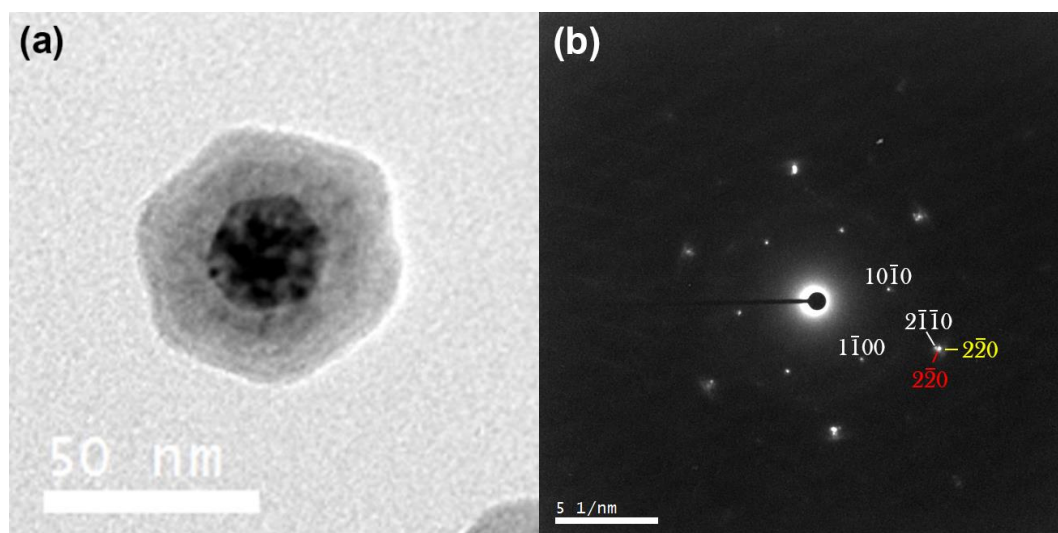


Figure 14: (a) High magnification bright field image of a core-shell $Mg_{85}Ti_{15}$ nanoparticle and (b) its correspond SAED pattern viewed along the Mg $[0001]$ axis. HCP Mg, FCC TiC and FCC MgO planes are indexed in white, red and yellow, respectively.

To investigate the role of Ti during nucleation and growth, a higher Ti content is obtained by increasing the sectioned target's composition from 50% to 75% Ti. The Mg-Ti nanoparticles that are grown in a methane gas environment show a noticeable different structural motif and crystal

structure with a composition of 66 ± 1 at% Mg. The particles are approximately 44 ± 6 nm and consist of a 22 ± 5 nm core, 8 ± 3 nm subshell enclosed as a whole in a 3-4 nm MgO shell. In addition, possibly carbon is deposited on several particles either due to excess methane usage during synthesis or due to carbon condensation under the electron beam in the TEM. A large number of nanoparticles have a porous subshell as shown in Figure 15, which was not observed previously for pure Mg nanoparticles of this relatively large size. Most likely the porosity originates from the oxidation related Kirkendall effect, such that the formation of an MgO shell consumes nearly all Mg.

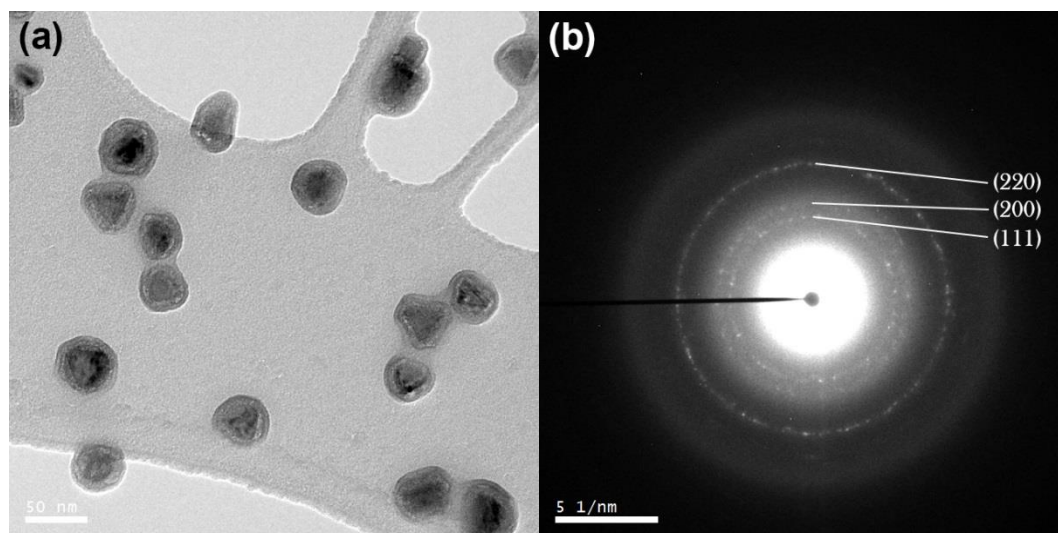


Figure 15: (a) Bright field image of $Mg_{66}Ti_{34}$ core-shell nanoparticles (b) and its corresponding SAED pattern.

The $Mg_{66}Ti_{34}$ nanoparticles have an FCC crystal structure deduced from the SAED pattern, as the $\{111\}$, $\{200\}$ and $\{220\}$ planes are identified leading to a lattice parameter of 4.42 ± 0.04 Å. This crystal structure matches with the TiC lattice. Remarkably, no planes corresponding to the HCP Mg are visible in the SAED pattern.

A high magnification bright field TEM image is shown in Figure 16 combined with its SAED pattern. The triangular nanoparticle is viewed along the $[111]$ direction as the TiC $\{220\}$ planes are resolved. This hints to faceting of the TiC core by $\{111\}$ or $\{100\}$ planes such that a tetrahedral shape is formed. The tetrahedron is capped by two $\{111\}$ planes which are parallel to the substrate as frequently trapezium shaped nanoparticles are observed i.e. viewed orthogonal to the $[111]$ direction. The surface energy of the TiC $\{100\}$ planes are generally predicted to be lower than the $\{111\}$ planes, owing to the alternating layers of C and Ti which result in polar surfaces in the latter case. However, this only holds in the stoichiometric case. For decreasing stoichiometry, the $\{111\}$ planes eventually become the most stable surfaces [46]. The surface energy of these planes directly impacts the growth rates e.g. the equilibrium shape determined by the Wulff construction depends on the ratio of the respective surface energies. Thus, at high stoichiometry the $\{100\}$ planes grow fastest, leaving the particle faceted by $\{111\}$ planes. Whereas at low stoichiometry the $\{111\}$ planes grow fastest such that the particle's facets are $\{100\}$ planes [47]. Since the dispersion of Ti in the nanoparticle is not known, the exact stoichiometry of TiC cannot be calculated properly based on the EDX results. Hence, determining the facets of the TiC core remains uncertain. Note that at $1/3^{\text{th}}$ TiC $\{422\}$ distance very subtle reflections are visible, which is a common feature for triangular nanoparticles and is believed to originate from defects such as twinning and stacking faults [48]–[51]. Due to a thin defect layer parallel to the substrate, the reciprocal lattice contains large rods which easily intersect with

the Ewald sphere to produce diffraction reflections. Furthermore, a stacking fault is proposed to be responsible for the plate like shape of the nanoparticles, as growth along the stacking fault plane is believed to be fastest [51].

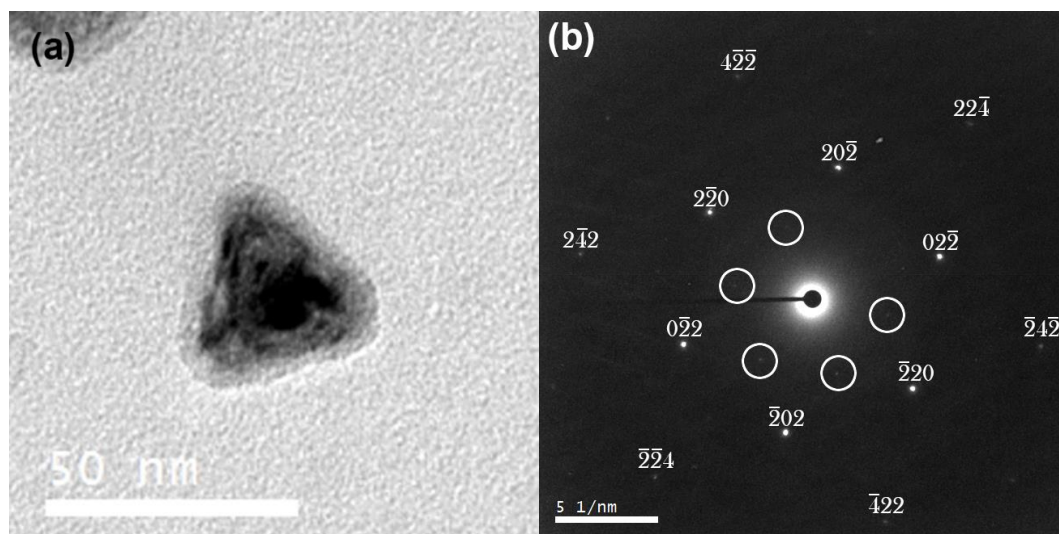


Figure 16: (a) High magnification bright field TEM image of a triangular $\text{Mg}_{66}\text{Ti}_{34}$ nanoparticle in projection (b) single nanoparticle SAED pattern viewed along the TiC $[111]$ axis. Note that very faint spots at $1/3\{422\}$ are circled.

Increasing the Ti content even more to obtain Mg-Ti nanoparticles with a composition of 45 ± 1 at% Mg yields smaller nanoparticles of 27 ± 5 nm, as shown in Figure 17. The shape of the nanoparticles appears very similar to the $\text{Mg}_{66}\text{Ti}_{34}$ ones. On top of the similar shape, the structural motif is also rather similar i.e. a 20 ± 3 nm core surrounded by a thin subshell and enclosed as a whole in a 2-3 nm MgO shell. Most clearly the Mg subshell has reduced in thickness as an effect of the decreased aggregation length which was necessary to obtain a Ti-rich composition. Moreover, the SAED pattern is identical to the $\text{Mg}_{66}\text{Ti}_{34}$ nanoparticles as the $\{111\}$, $\{200\}$, $\{220\}$ and $\{311\}$ planes of an FCC lattice are resolved with a lattice parameter of $4.42 \pm 0.04 \text{ \AA}$. Again, this lattice corresponds to a FCC TiC crystal structure, where no HCP Mg is present.

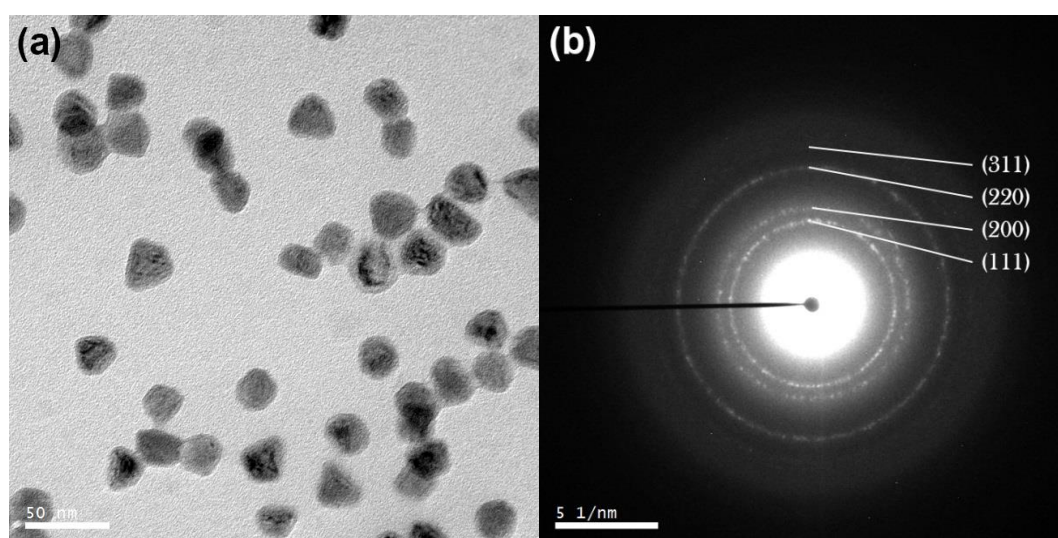


Figure 17: (a) Bright field TEM image of $\text{Mg}_{45}\text{Ti}_{55}$ nanoparticles grown in an Ar- CH_4 gas environment (b) and its corresponding SAED pattern.

Clearly, nucleation and growth of Mg-Ti nanoparticles is affected by addition of methane gas in the aggregation chamber. Although great control over nucleation rate is achieved through a controlled flow of methane, several effects cannot be prevented. Synthesis of Mg-Ti nanoparticles in an Ar-CH₄ gas environment results in the formation of core-shell nanoparticles. Closer inspection reveals the core to be FCC TiC with a lattice parameter of $4.42 \pm 0.04 \text{ \AA}$, and the shell is HCP Mg with lattice parameters of $a = 3.22 \pm 0.03 \text{ \AA}$ and $c = 5.16 \pm 0.05 \text{ \AA}$. On top of that, the formation of TiC is independent of the composition of the Mg-Ti nanoparticles. This can be deduced from the observation that Mg-Ti nanoparticles with a composition ranging from Mg₄₅Ti₅₅ to Mg₈₅Ti₁₅ all yield the presence of an FCC crystal structure as determined from SAED patterns. Despite the presence of Mg, no HCP Mg is observed for the Mg₆₆Ti₃₄ and Mg₄₅Ti₅₅ nanoparticles as only the TiC FCC crystal structure is observed in SAED, which strongly suggests that Mg is present only in the MgO shell. The faceting of the nanoparticle core is affected by changing the Mg/Ti ratio as is noted by the change of shape. For the Mg-rich nanoparticles the surfaces are mainly the $\{10\bar{1}1\}$ and $\{0002\}$ planes of Mg, while the particle is faceted by $\{111\}$ or $\{100\}$ planes of TiC when less Mg is present. These results point to the growth of Mg on the TiC core that subsequently oxidized to form an outer MgO shell. At a high Mg concentration a significant amount of HCP Mg remains whereas virtually all HCP Mg is consumed by the oxide formation at lower Mg concentrations.

Addition of methane gas during synthesis is a conventional method to produce TiC thin films or nanoparticles [47], [52]–[54]. The nucleation and growth of these nanoparticles can be explained by either homogeneous or heterogeneous nucleation, or a combination of both. In the former mechanism methane decomposes in the plasma to carbon and hydrogen such that the supersaturated Ti vapour homogeneously nucleates in an Ar-C gas to form TiC clusters. Despite decomposing in four hydrogen atoms and only one carbon atom, TiC is formed most likely due to the lower (more negative) Gibb's free energy of TiC (-180 kJ/mol [55]) compared to TiH₂ (-113 kJ/mol [56]). Alternatively, TiC nucleation could be explained due to target poisoning and heterogeneous nucleation [54]. At sufficiently high partial pressure of methane, carbon adsorbs on the Ti target and forms a thin TiC surface layer on top of the Ti target. This effect is supported by the fact that the sputtering voltage increases several tenths of volts at the moment when the target is subjected to a methane gas flow. An increased sputter voltage indicates that more energetic Ar ions have to compensate for the increased binding energy of surface atoms i.e. TiC has got a lower sputter yield compared to Ti due to the covalent/ionic character of TiC. Moreover, nucleation continuous for several seconds when methane is evacuated from the system, that indicates the erosion of a contaminated surface layer. During cooling and transport by the Ar gas flow Mg condenses on the TiC seeds to form a core-shell particle, since high melting point materials tend to nucleate first [16]. The presence of Ti in the Mg shell is likely as the shape of the Mg-rich nanoparticle is faceted by $\{10\bar{1}1\}$ and $\{0002\}$ planes which are low surface energy planes for a Ti crystal. The growth of Mg on TiC is supported by the observation that the TiC core diameter remains approximately 20-25 nm whereas the Mg shell reduces in size when the composition of the nanoparticles becomes richer in Ti.

4.2.3 Synthesis in an Ar-H₂ gas environment

Hydrogen gas has been used during synthesis to further investigate the effect of the gas environment on the synthesis of Mg-Ti nanoparticles. Moreover, the aim of the different impurity gas is to achieve alloyed nanoparticles which are more desirable for hydrogenation than the ones containing a TiC core. The Ti content in the nanoparticles is increased by changing the sectioned target's composition

from 50% to 75% Ti and by changing the length of the aggregation chamber. Having a composition of 64 ± 1 at% Mg and 36 ± 1 at% Ti yields nanoparticles with a size of 28 ± 7 nm. The Mg-Ti nanoparticles form a core-shell structural motif with a core diameter of 22 ± 3 nm and a 3-5 nm shell, with significant amount of void formation leading to a porous subshell (Figure 18). The size distribution is rather broad as the shape of the nanoparticles has an aspect ratio below unity. As a result of projection along the two orthogonal directions the size distribution approaches a bimodal distribution leading to broadening of the peak. The thickness of the platelets is approximately 17 ± 3 nm and the diameter 35 ± 5 nm.

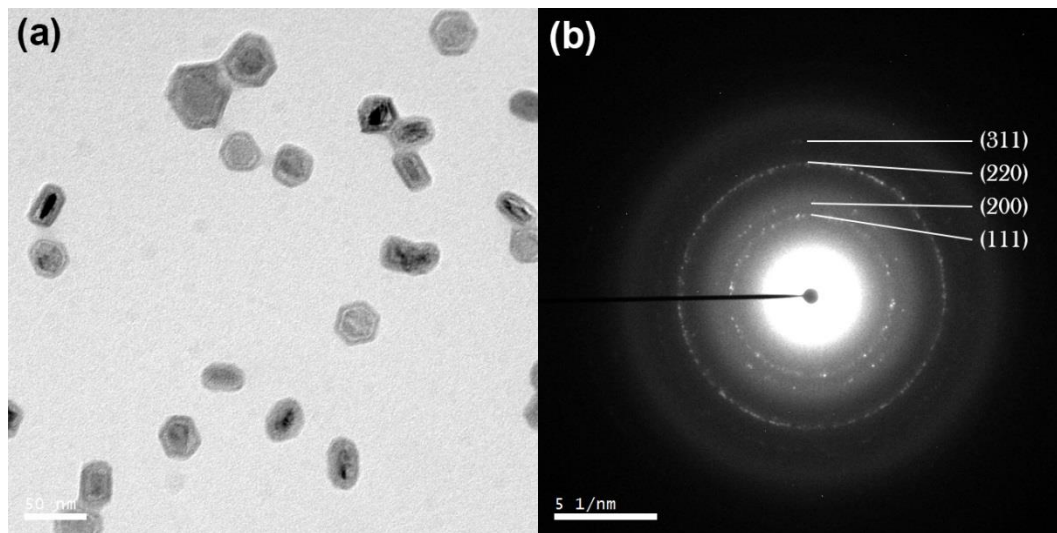


Figure 18: (a) Bright field TEM image of $Mg_{64}Ti_{36}$ nanoparticles grown in an Ar- H_2 environment (b) its corresponding SAED pattern.

In the SAED pattern the $\{111\}$, $\{200\}$, $\{220\}$ and $\{311\}$ planes are resolved which yields a cubic crystal structure with FCC symmetry with a lattice parameter of 4.53 ± 0.05 Å. This crystal structure most probably corresponds to a fluorite FCC TiH_2 lattice which is formed *in-situ* as a consequence of injected molecular hydrogen gas. Besides the allowed planes for the FCC crystal structure no reflections corresponding to a HCP crystal can be identified. Even though having 64 ± 1 at% Mg there appears to be not sufficient HCP Mg crystals to be observed in diffraction. Possible causes for this observation are an alloyed Mg-Ti with an FCC structure or the oxidation associated Kirkendall effect that has consumed virtually all HCP Mg.

Bright field TEM images indicate that the nanoparticles have a preference to form hexagonal prism like shapes, as the projected shape is either a hexagon or a rectangle. This suggests that the nanoparticles have two preferential orthogonal facets to land on the substrate. Single nanoparticle SAED has been employed to obtain SAED patterns from two orthogonal directions which allow the particle's orientation to be determined, as shown in Figure 19. The nanoparticle is hexagonal in projection as viewed along the cubic $[111]$ direction. Along this direction the $\{220\}$ planes are resolved which are parallel to the hexagon's vertices. Based on the SAED pattern and symmetry the facets of the particle can be $\{111\}$ planes to form a tetrahedral shape of which the vertices are truncated by $\{100\}$ planes, or vice versa. The truncation by the $\{100\}$ and $\{111\}$ planes is further supported by the observation that many particles have a truncated triangular shape as the $\{111\}$ and $\{100\}$ planes are not at the same distance from the center. In addition, viewing along the $[11\bar{2}]$ direction yields a rectangular shape in projection where the $\{111\}$ and $\{220\}$ planes are visible. Hence, the particle is capped on top and bottom by two $\{111\}$ planes and the side faces are $\{111\}$ and $\{100\}$ planes. This crystal shape has been observed for many FCC metallic nanoparticles such as Pd, Ni-Cu and Au [48]–[50]. Based on DFT calculations the TiH_2 (111) plane has nearly half the surface energy compared to the (100) plane, which supports the observation that the nanoparticles are predominantly faceted by $\{111\}$ planes [45].

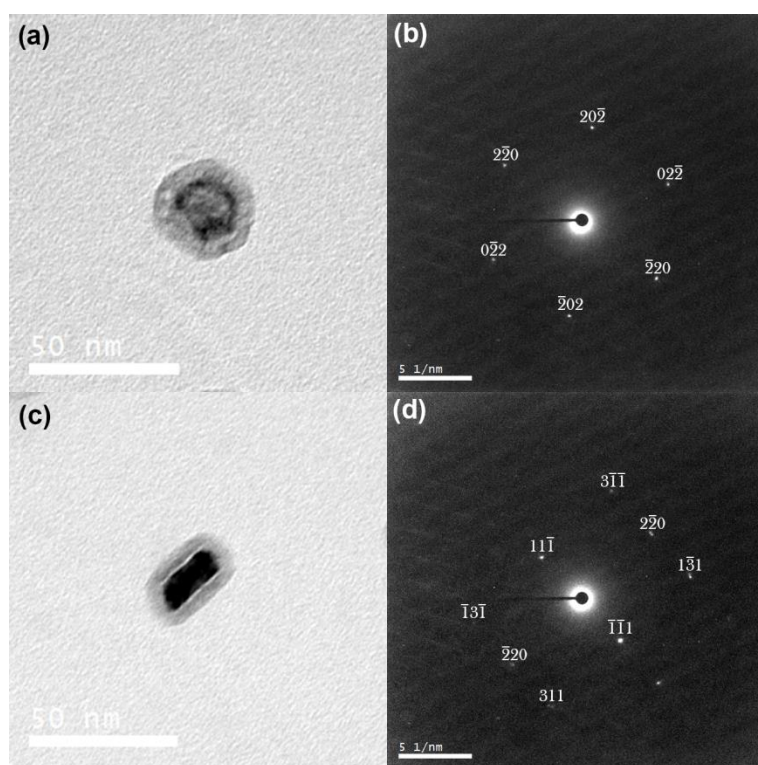


Figure 19: High magnification bright field TEM images and SAED patterns of $\text{Mg}_{64}\text{Ti}_{36}$ nanoparticles which are (a) hexagonal in projection viewed along (b) the $[111]$ axis, and (c) rectangular in projection viewed along (d) the $[11\bar{2}]$ axis.

Nanoparticles with a higher Ti content are shown in Figure 20 and have been synthesized by decreasing the aggregation length; these nanoparticles have a composition of 47 at% Mg and a mean diameter of 24 ± 5 nm. No clear shell is observed besides the 3-4 nm thick MgO shell, which indicates the formation of an alloyed structure. At high magnification void development beneath the MgO shell is observed which in some occasions led to a porous subshell, which can be explained by the oxidation associated Kirkendall effect. The SAED pattern reveals the $\{111\}$, $\{200\}$ and $\{220\}$ planes

such that the crystal structure is determined to be FCC with a lattice parameter of $4.45 \pm 0.05 \text{ \AA}$ which corresponds to the fluorite TiH_2 crystal structure. Yet again, the low index HCP Mg planes are not visible in the SAED pattern. The shape of the nanoparticles tend to be platelet like since the projections either form a disk or a rectangle, which is very similar to the nanoparticles described before. However, the exact faceting cannot be determined as the particles do not have sharp facets as the previous nanoparticles.

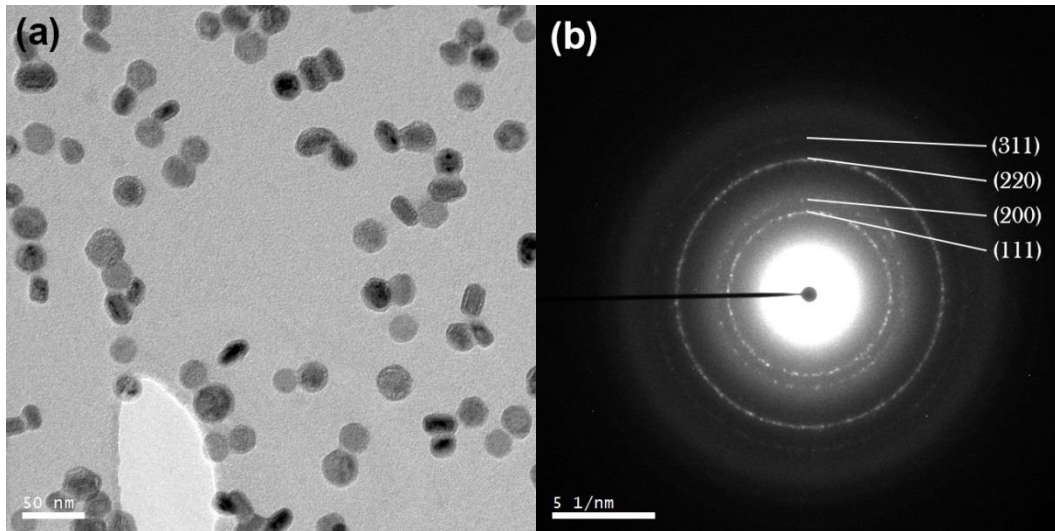


Figure 20: (a) Bright field TEM image of $\text{Mg}_{47}\text{Ti}_{53}$ nanoparticles grown in an Ar- H_2 environment (b) its corresponding SAED pattern.

Hence, the Mg-Ti nanoparticles synthesized in an Ar- H_2 gas environment form a TiH_2 crystal structure as a result of *in-situ* hydrogenation of Ti. In bright field TEM images there are clear signs of void formation beneath the MgO shell which point to the oxidation related Kirkendall effect. The formation of MgO nearly consumes all HCP Mg, such that this cannot be resolved in SAED patterns. Especially in the more Mg-rich (around 70 at% Mg) nanoparticles the porous subshell is visible, which shrinks in size for the Ti-rich (around 50 at% Mg) particles. Therefore, this suggests the growth of HCP Mg on the TiH_2 core that oxidizes to form the MgO shell. However, the formation of a TiH_2 crystal structure of a solid solution of Mg and Ti has been reported for thin film systems. Therefore, not necessarily all Mg is present in the MgO shell, but also possibly in an alloyed form in the core.

4.2.4 Oxidation associated Kirkendall effect

When the Mg-Ti nanoparticles are synthesized with methane or hydrogen as impurity gas, Mg will always grow on the TiC or TiH₂ core such that the outer Mg shell is exposed and will oxidize. Since MgO growth is a diffusion limited process, the MgO thickness is limited to 3-4 nm. Therefore, in any case Mg is supplied to the oxidation reaction such that a loss of Mg is inevitable. Hence, whenever the volume of Mg required for the MgO growth compares with the available Mg in the subshell, void development leads to a porous or even hollow Mg subshell. This effect is clearly visible when the Mg-Ti nanoparticles' size reaches 20 nm or smaller. Void formation occurs already *in-situ* and during transfer to the TEM (Figure 21).

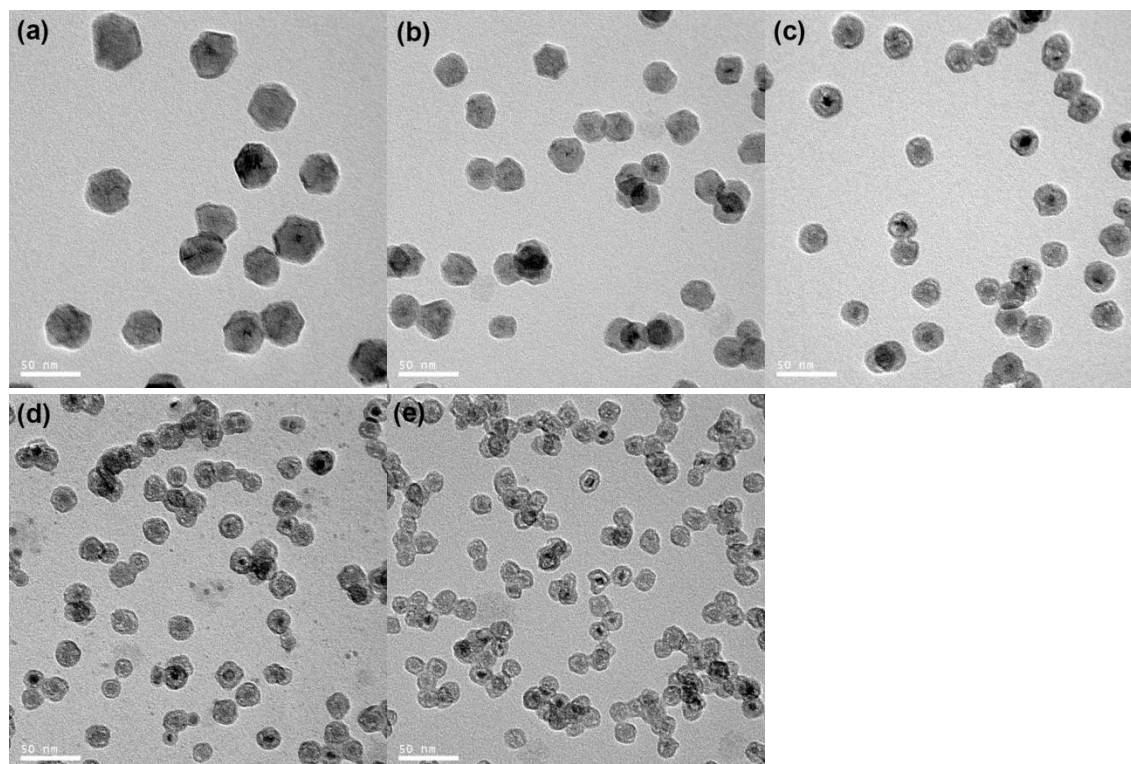


Figure 21: Void formation in Mg-Ti nanoparticles due to the oxidation related Kirkendall effect where the nanoparticle size is (a) 36±4 nm (b) 26±5 nm (c) 22±4 nm (d) 19±6 nm (e) 17±7 nm.

The voids form especially near the Mg/MgO interface, resulting in a TiC/TiH₂ core surrounded by a porous Mg subshell as a whole enclosed in a thin MgO shell. For relatively large nanoparticles (diameter >30 nm) oxidation does not lead to severe void formation, however over time the MgO shell does show inward relaxation suggesting the loss of Mg as shown in Figure 22. This effect can explain why HCP Mg is not present in the smaller nanoparticles produced with a reduced Mg concentration. In this case the Mg shell that has grown on the core has a molar volume that compares very well with the molar volume of the MgO shell, such that nearly all Mg atoms are transported to the MgO shell. Therefore, the Mg subshell has a porous structure and in some cases is essentially hollow. Remarkably, this effect is more pronounced for particles produced with hydrogen compared to synthesis in methane.

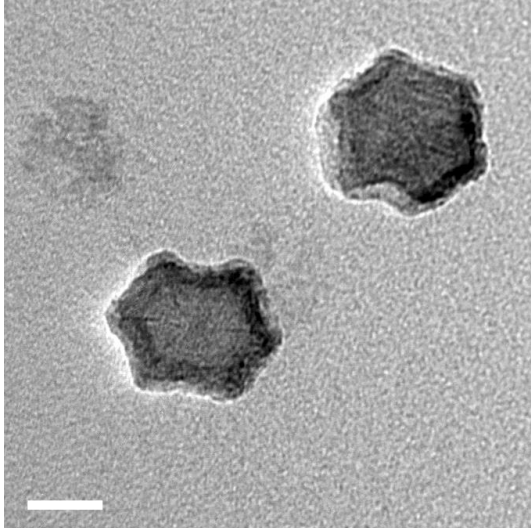


Figure 22: Inward relaxation of the MgO shell of nanoparticles shown in Figure 21a nearly three months after synthesis. The nanoparticles were predominately stored in vacuum (10^{-2} mbar), but were exposed to air during transfer to the TEM. Note that near the nanoparticles island have grown which could be redeposited magnesium.

To reduce the transport of Mg, the MgO shell has to be made as thin as possible. The thin MgO shell is the result of sharp Mg-Ti facets that allow uniform growth of the MgO layer such that only a thin MgO shell is capable of enclosing the Mg-Ti nanoparticle. The thin MgO shell requires less Mg transport over the interface such that void nucleation and clustering in the Mg subshell can be minimized. Thus, Mg-Ti nanoparticles that are sharply faceted have the potential to grow a relatively thin MgO shell which is desired to minimize void formation as a result of the oxidation associated Kirkendall effect [12].

4.3 Hydrogenation of Mg-Ti nanoparticles

4.3.1 Thermal competition of hydride formation and Mg evaporation

Hydrogenation of Mg-Ti nanoparticles requires the correct circumstances to provide a thermodynamically driving force for hydride formation. This is achieved by applying a molecular hydrogen gas pressure that exceeds the estimated MgH_2 equilibrium pressure substantially. As described by the Van 't Hoff equation (Equation 4) this yields a negative Gibb's free energy such that the hydrogenation reaction is stimulated. Although MgH_2 formation is thermodynamically favourable under these conditions, there are many processes that require additional thermal energy to overcome potential barriers e.g. molecular hydrogen dissociation on MgO, diffusion through the MgO shell, diffusion through Mg and diffusion through MgH_2 . To investigate the effect of the thermal energy on the hydrogenation of Mg-Ti nanoparticles, hydrogenation has been carried out at various temperatures ranging from 100 °C up to 250 °C under equal hydrogen pressure of 10 bar. The resulting TEM bright field images and SAED patterns are shown in Figure 23.

Alloyed 36 ± 4 nm $\text{Mg}_{88}\text{Ti}_{12}$ nanoparticles that have been hydrogenated at 100 °C for 72 hours, show no sign of a phase transition in the SAED pattern that indicates the formation of the α - or β - MgH_2 (Figure 23a). The SAED patterns of the *as-deposited* and hydrogenated nanoparticles are identical where the low index HCP Mg $\{10\bar{1}0\}$, $\{0002\}$ and $\{10\bar{1}1\}$ planes are resolved. Clearly, there is a high barrier amongst the processes required for atomic hydrogen penetration into the Mg lattice. Another effect, besides those involved for hydrogenation, is activated at this temperature, namely the evaporation of Mg to establish its equilibrium vapour pressure. In nearly all nanoparticles void formation has occurred due to Mg evaporation. Evaporation of Mg as the cause of the voids is supported by the observation that many smaller nanoparticles (< 20 nm) have become virtually completely hollow. Clustering of voids leads to larger voids at the Mg/MgO interface. Remarkably, voids are not present uniformly to form a porous subshell below the MgO; instead voids are developed on one particular side of the nanoparticle. In some occasions when the particle is sharply faceted the formation of voids at the MgO surface leads to inward relaxation of the MgO shell.

Therefore, alloyed $\text{Mg}_{81}\text{Ti}_{19}$ nanoparticles with a mean size of 26 ± 5 nm were hydrogenated at 150 °C for 5 hours to provide more thermal energy to the system in order to stimulate the hydrogenation processes (Figure 23b). Yet, under these circumstances the formation of the α - or β - MgH_2 is not observable in the SAED pattern. Furthermore, Mg evaporation cannot be prevented by the MgO shell that encloses the nanoparticles. Void formation occurred faster compared to hydrogenation at 100 °C for 72 hours. In this case 5 hours of annealing at 150 °C in the hydrogen gas environment yields approximately equally sized voids compared to annealing for 72 hours at 100 °C. The increased temperature and decreased particle size provides a higher driving force for Mg evaporation as described by the Kelvin equation (Equation 1). Possibly, Mg can be transported most easily through the vertices of the hexagonal nanoparticle, as at these location the MgO shell is not closed due to an misorientation of the MgO layers on adjacent Mg facets [12]. Mg evaporation is completely suppressed when the particles are larger than 30 nm.

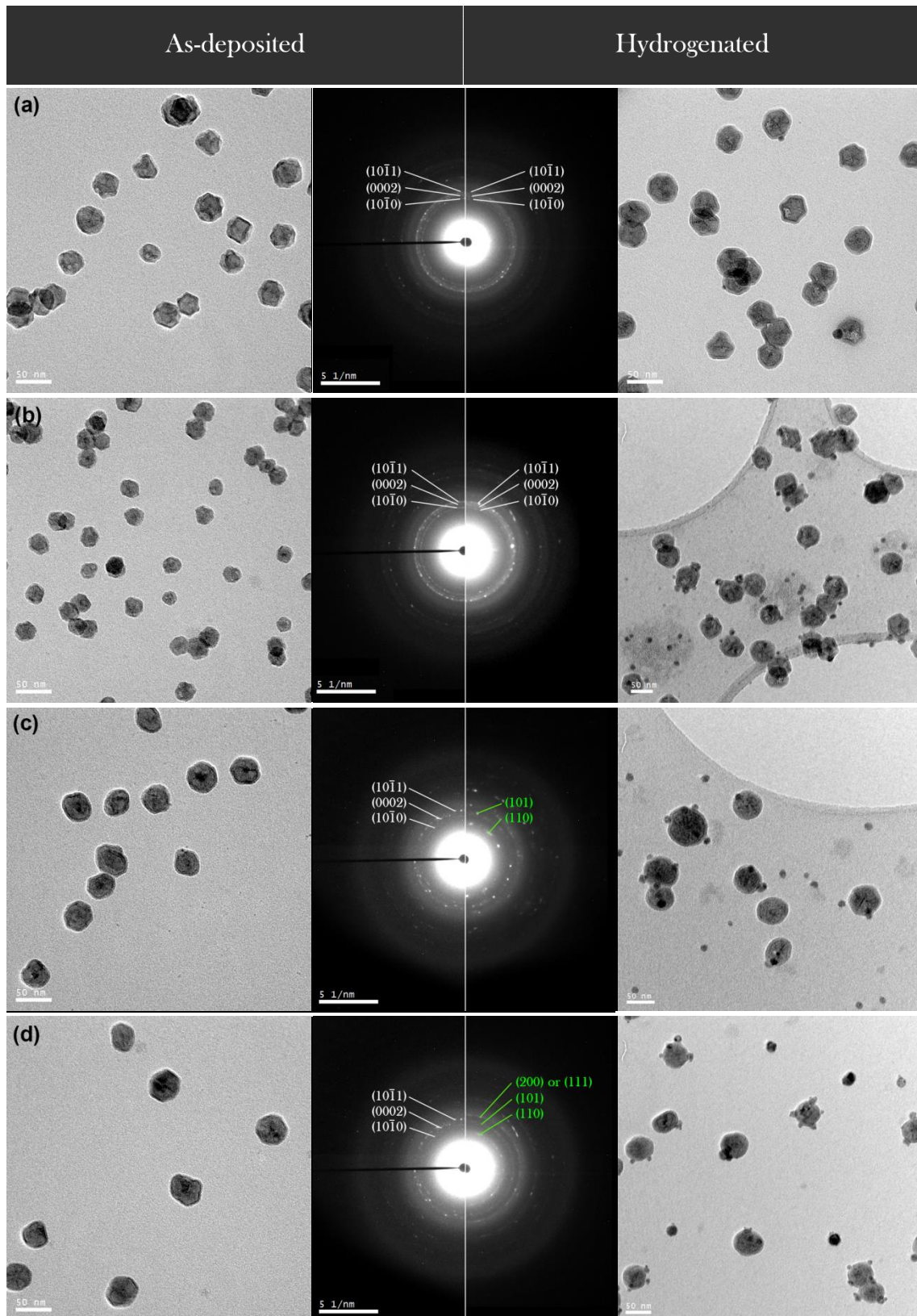


Figure 23: TEM bright field images of the *as-deposited* and hydrogenated alloyed Mg-Ti nanoparticles at various temperatures. (a) 100 °C for 72 hours (b) 150 °C for 5 hours (c) 200 °C for 2 hours (d) 250 °C for 2 hours. The left column shows the *as-deposited* nanoparticles and the column at the right shows the hydrogenated nanoparticles. The SAED patterns of the *as-deposited* nanoparticles is shown in the left half of the middle column, and the SAED pattern of the hydrogenated nanoparticles is shown in the right half of the middle column. Planes of Mg and MgH₂ are indexed in white and green, respectively.

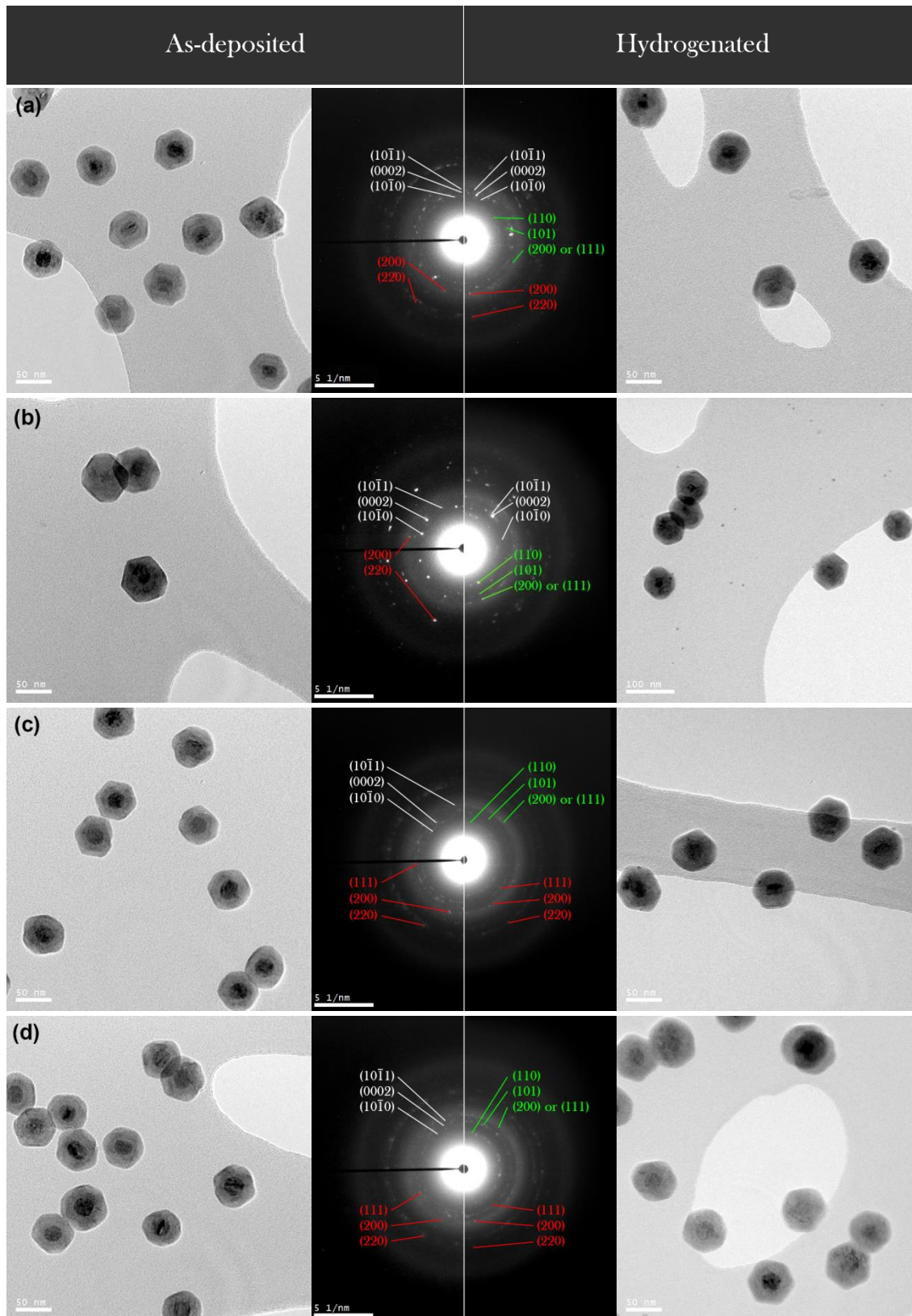


Figure 24: TEM bright field images of the *as-deposited* and hydrogenated core-shell TiC-Mg nanoparticles at various temperatures. (a) 150 °C for 2 hours (b) 175 °C for 2 hours (c) 200 °C for 2 hours (d) 250 °C for 2 hours. The left column shows the *as-deposited* nanoparticles and the column at the right shows the hydrogenated nanoparticles. The SAED patterns of the *as-deposited* nanoparticles is shown in the left half of the middle column, and the SAED pattern of the hydrogenated nanoparticles is shown in the right half of the middle column. Planes of Mg, MgH₂ and TiC are indexed in white, green and red, respectively.

TiC-Mg core-shell nanoparticles with a composition of 86 ± 1 at% Mg and 14 ± 1 at% Ti with a mean size of 56 ± 3 nm have a thin MgO shell that encloses the hexagonally shaped particles. Hydrogenation at 150°C for 2 hours does not result in void formation at the Mg/MgO interface. In contrast, the body-centered tetragonal (BCT) β -MgH₂ crystal structure (also called the rutile structure) is coexisting with HCP Mg as identified from the SAED pattern (Figure 24a). In the SAED pattern the low index $\{110\}$, $\{101\}$ and $\{200\}$ or $\{111\}$ planes of the β -MgH₂ crystal structure are resolved in addition to the low index HCP Mg $\{10\bar{1}0\}$, $\{0002\}$ and $\{10\bar{1}1\}$ planes. Note that the β -MgH₂ $\{200\}$ interplanar spacing could also be indexed as the $\{111\}$ reflection which is normally forbidden for the BCT MgH₂ lattice. This can indicate that the lattice is not saturated with hydrogen atoms to completely suppress the forbidden $\{111\}$ reflection. However, it also means that no $\{200\}$ reflection occurs, which implies ordering in the lattice such that the $\{200\}$ reflection is diminished and the $\{111\}$ reflection is no longer forbidden i.e. indexing the $\{200\}$ or $\{111\}$ planes is difficult. The lattice parameters of the BCT β -MgH₂ crystal are $a=4.68\pm 0.05$ Å and $c=3.08\pm 0.03$ Å, which is slightly larger than often reported in literature [24], [57]. In the bright field TEM images a 7 ± 5 nm shell of β -MgH₂ is visible which is not uniform in thickness. The presence of β -MgH₂ as a subshell is supported by the HRTEM image in Figure 25, where the (110) β -MgH₂ planes are resolved.

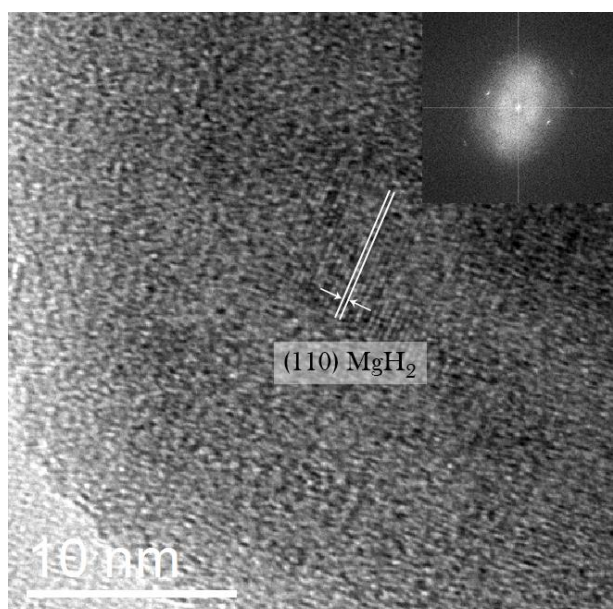


Figure 25: HRTEM bright field image where the (110) planes of the rutile MgH₂ phase are resolved in the nanoparticle's shell; the FFT is shown in the inset.

Hence, Mg evaporation can be prevented by ensuring the nanoparticles are rather large and by supplying sufficient thermal energy to provide driving force for the hydrogenation sequence. Increasing the temperature during hydrogenation up to 175°C also lead to the nucleation of the BCT β -MgH₂ in core-shell Mg₈₈Ti₁₂ nanoparticles with a mean diameter of 64 ± 3 nm. Due to the significantly larger diameter the driving force for Mg evaporation is reduced and hydrogen is capable of penetrating the MgO shell and diffusing into the bulk Mg of the nanoparticles. From the SAED pattern HCP Mg and β -MgH₂ are identified by their low index planes i.e. Mg $\{10\bar{1}0\}$, $\{0002\}$ and $\{10\bar{1}1\}$ and β -MgH₂ $\{110\}$, $\{101\}$ and $\{200\}$ or $\{111\}$ (Figure 24b).

Hydrogenation has been carried out at higher temperatures such as 200°C and 250°C to further investigate the effect of thermal energy on the hydrogenation and Mg evaporation processes. Under

these conditions no voids are observed near the Mg/MgO interface for alloyed (Figure 23c,d) and core-shell nanoparticles (Figure 24c,d). Furthermore, no sign of HCP Mg is apparent from the SAED pattern as only planes corresponding to the BCT MgH₂ are visible. After hydrogenation the alloyed nanoparticles remain in their alloyed state i.e. hydride formation of the alloyed Mg-Ti crystal structure does not impose stringent thermodynamic driving force for phase segregation which can occur on the timescale of the hydrogenation reaction. Also the TiC-Mg core-shell nanoparticles maintain their structural motif after hydrogenation, such that only the Mg shell is capable of absorbing hydrogen to form the β -MgH₂ phase. This is apparent from the SAED pattern as BCT β -MgH₂ planes are identified in addition to FCC TiC planes. Sub-stoichiometric TiC is capable of absorbing hydrogen, as the alternating {111} planes of carbon contain vacancies which can be occupied by hydrogen atoms. However, there is only little influence on the lattice parameter of the FCC cubic structure such that this cannot be distinguished in the SAED pattern [58].

This suggests that hydride formation and Mg evaporation are competing processes which can be thermally controlled. Molecular hydrogen dissociation rate, MgO penetration and atomic hydrogen diffusion increases when sufficient thermal energy is supplied to the molecular hydrogen gas and the nanoparticles. Atomic hydrogen rapidly diffuses in the Mg-Ti lattice and supersaturates such that the β -MgH₂ phase nucleates. Nucleation of the β -MgH₂ phase occurs at the Mg/MgO interface, as supersaturation of the α -MgH₂ phase is first reached at this location. In addition, the MgO shell provides heterogeneous nucleation sites for the β -MgH₂ phase such that further growth by β -MgH₂ coalescence leads to the formation of a β -MgH₂ shell [34]. The β -MgH₂ shell acts as a diffusion barrier for Mg which prevents Mg evaporation. Further hydrogenation requires the diffusion of atomic hydrogen through the β -MgH₂ shell and supersaturation of the remaining HCP Mg-Ti.

Thus, both Mg evaporation and hydride formation are processes that are kinetically blocked by several barriers. At relatively low temperature (< 150°C) no hydride can be formed which therefore cannot prevent Mg evaporation. The driving force of Mg evaporation is described by the Kelvin equation (Equation 1) such that smaller particles provide a larger thermodynamic driving force for Mg evaporation [10]. When the particles are relatively large (> 50 nm) the thermodynamic driving force is many orders of magnitude lower and no voids are developed due to Mg evaporation at 150 °C. As the temperature reaches higher values (> 175°C) molecular hydrogen dissociation, MgO penetration and Mg diffusion reach a higher rate such that supersaturation of atomic hydrogen is achieved leading to the formation of a blocking β -MgH₂ shell. At this point Mg transport rate is diminished and evaporation can be prevented.

4.3.2 Influence of Ti concentration on the hydride crystal structure

By controlling the Ti content in Mg-Ti thin film alloys, the hydride structure varies from a rutile type MgH_2 to a fluorite type TiH_2 [22], [23], [57], [59]. Typically the fluorite Mg-Ti hydride structure is expected to have superior hydrogenation kinetics due to faster diffusion in the hydride [57], [60], [61]. Hence, this is a desired effect to improve hydrogen sorption kinetics. Hydrogenation results in the formation of MgH_2 and locally TiH_2 clusters i.e. the system is neither a random alloy nor phase segregated. In fact partial phase segregation is believed to lead to Mg-rich and Ti-rich regions in the alloy due to spinodal like phase separation. Since hydrogen first occupies the Ti-related sites due to the lower formation enthalpy, the intermediate system consist of fluorite TiH_2 clusters in a HCP Mg matrix. Further hydrogenation leads to rutile MgH_2 along TiH_2 clusters when the Ti concentration is low. At higher overall Ti concentration the coherent interface between the fluorite TiH_2 and HCP Mg forces the formation of a fluorite Mg-Ti-H alloy. The transition from the rutile MgH_2 to fluorite TiH_2 crystal structure generally occurs in the range of 80-90 at% Mg [22], [23], [59].

Figure 26 shows hydrogenated nanoparticles produced in an Ar- CH_4 gas environment with a varying composition ranging from 45 to 84 at% Mg. Hydrogenated nanoparticles with a Mg-rich composition (84 at% Mg) form the rutile MgH_2 crystal structure as $\{110\}$, $\{101\}$ and $\{200\}$ or $\{111\}$ planes are resolved, accompanied with a TiC core (Figure 26a,d). When the nanoparticles possess less Mg with a composition of 45 or 66 at% Mg, they have an FCC crystal structure in the *as-deposited* state, where no HCP Mg is observed. The $\text{Mg}_{66}\text{Ti}_{34}$ nanoparticles (Figure 26b,e) have an initial lattice parameter of $4.42 \pm 0.04 \text{ \AA}$ which remains approximately equal at $4.38 \pm 0.04 \text{ \AA}$ after hydrogenation. The $\text{Mg}_{45}\text{Ti}_{55}$ nanoparticles (Figure 26c,f) show similar results where the *as-deposited* crystal structure is FCC with a lattice parameter of $4.42 \pm 0.04 \text{ \AA}$ and hydrogenated nanoparticles have an FCC crystal structure with a lattice parameter of $4.45 \pm 0.04 \text{ \AA}$.

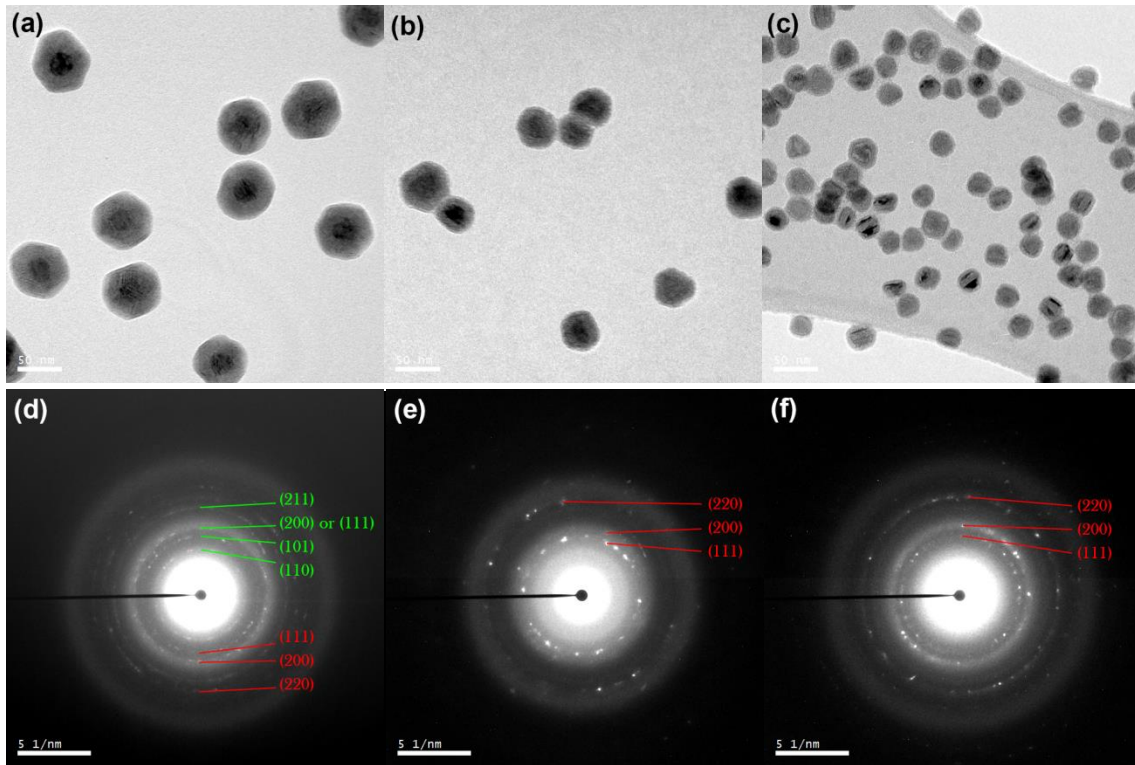


Figure 26: TEM bright field images and SAED patterns of the hydrogenated Mg-Ti nanoparticles synthesized in Ar-CH₄ with a composition of (a,d) 84 at% Mg (b,e) 66 at% Mg (c,f) 45 at% Mg. The MgH₂ and TiC reflections are indexed in green and red, respectively.

A similar effect occurs when the nanoparticles are produced in an Ar-H₂ gas environment. The Mg₆₄Ti₃₆ nanoparticles have an *as-deposited* FCC crystal structure with a lattice parameter of 4.53±0.05 Å. Hydrogenation leads to the formation of rutile MgH₂ as the {110} planes in addition to TiH₂ of which the {111} and {220} planes are resolved (Figure 27a,c), although the intensities are rather poor due to the use of a small selected area aperture. Possibly, the Mg-Ti nanoparticles were hydrogenated *in-situ* in the nanocluster source having an alloyed structure, which phase segregated during the subsequent hydrogenation process due to the supplied thermal energy. The *as-deposited* samples show void formation by the presence of a porous subshell, where the voids further cluster during hydrogenation. No substantial Mg evaporation occurred as the composition measured by EDX remained approximately equal. Hence, the presumable *as-deposited* alloyed FCC Mg-Ti-H crystal structure does not retain after hydrogenation as phase segregation in BCT MgH₂ and FCC TiH₂ occurs.

The nanoparticles with a lower Mg concentration of Mg₄₇Ti₅₃ also have an *as-deposited* FCC crystal structure due to synthesis in an Ar-H₂ gas environment. The lattice parameter is 4.45±0.05 Å as calculated from the SAED pattern which matches the TiH₂ crystal structure. After hydrogenation the FCC lattice expands to reach a lattice parameter of 4.86±0.05 Å (Figure 27b,d). This lattice parameter is substantially larger than expected for a fluorite TiH₂ lattice, but has been observed in Mg-Ti thin films. The {111} interplanar spacing of the fluorite crystal increased significantly as a function of hydrogen uptake for a thin film Mg-Ti alloy with a composition of Mg₇₀Ti₃₀. This effect was attributed to the sequential hydrogenation of Ti-rich and Mg-rich regions. Initially, the Ti-rich regions absorb hydrogen due to the lower enthalpy followed by filling the Mg-rich regions such that the lattice expands significantly during hydrogenation [62]. Therefore, this observation hints towards the alloyed structure of Mg-Ti in nanoparticles with a Ti-rich composition.

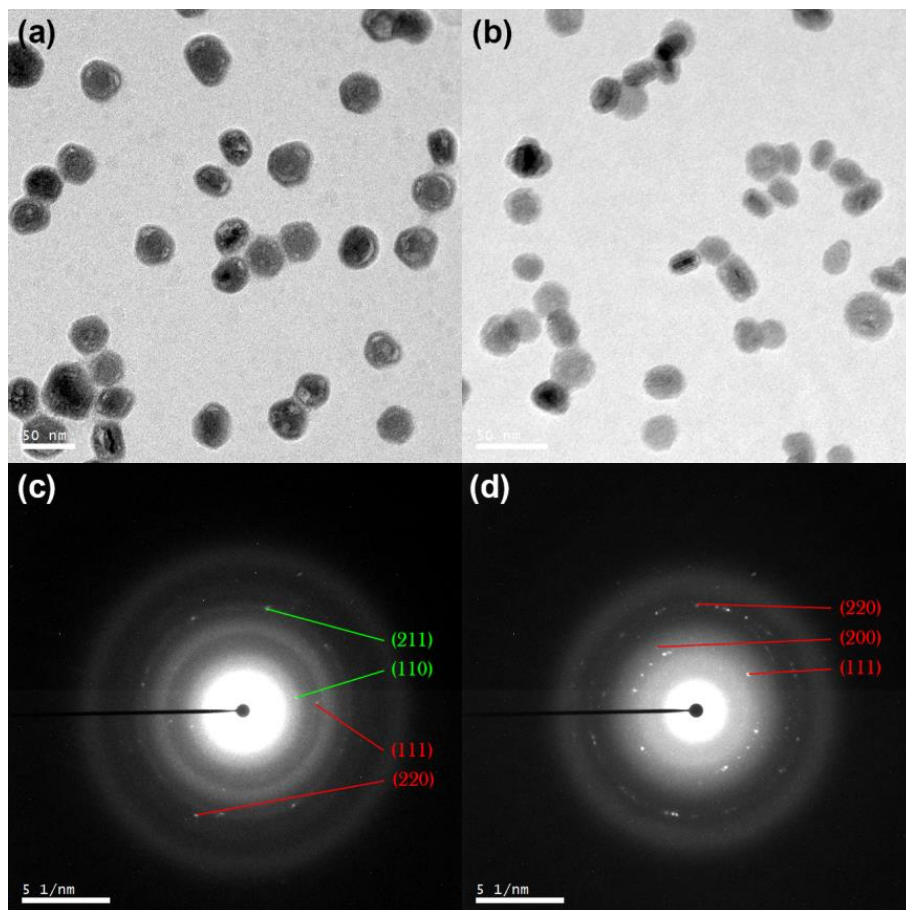


Figure 27: TEM bright field images and SAED patterns of the hydrogenated Mg-Ti nanoparticles synthesized in Ar-H₂ with a composition of (a,c) 64 at% Mg (b,d) 47 at% Mg. The MgH₂ and TiH₂ planes are indexed in white and red, respectively.

Unlike the very similar *as-synthesized* nanoparticles produced with hydrogen or methane added to the Ar sputtering gas, the result of hydrogenation on the crystal structure is different. For a composition close to 70 at% Mg the results show phase segregation of fluorite TiH₂ and rutile MgH₂ when hydrogen was used during synthesis. In contrast, no rutile MgH₂ is observed in the SAED pattern when synthesized with methane addition. With a Ti-rich composition with over 50 at% Ti, the nanoparticles produced with hydrogen gas show a significant increase in lattice parameter of the FCC fluorite crystal structure, whereas the lattice parameter remains constant for nanoparticles created with methane. Therefore, these observations suggest that the alloyed Mg-Ti(C)-H structure retains during hydrogenation when the composition is rich in Ti (over 50 at% Ti).

The hydride crystal structure of the entire nanoparticle depends on the composition, i.e. compositional tuning between the rutile and fluorite crystal structure is possible. In any case, Ti reacts with the methane or hydrogen gas to form TiC or TiH₂, respectively. If the Mg shell is relatively thick (Mg-rich composition), HCP Mg is present in the *as-deposited* nanoparticles and the rutile MgH₂ is formed when hydrogenated. However, thinner shells (less Mg-rich) are not capable of forming a HCP Mg crystal structure in the *as-deposited* state such hydrogenation results in the formation of solely TiH₂. Hence, although the particles are not forming an alloyed structure, but rather core-shell particles with possibly a slight amount of alloying, the rutile to fluorite transition is also observed in these nanoparticles at much higher Ti concentrations compared to literature.

4.3.3 Surface nucleation of Copper nanoparticles

As a side effect of hydrogenation at elevated temperature, additional small nanoparticles appear to nucleate on the holey carbon substrate surface. Hydrogenation carried out at 150 °C for 72 hours results in the growth of nanoparticles of approximately 6 nm. Many of these nanoparticles are distributed around the Mg-Ti nanoparticles instead of being randomly distributed over the holey carbon substrate. Increasing the temperature results in larger nanoparticles i.e. during annealing the nanoparticles nucleate and grow on the substrate. The nanoparticle density increases significantly close to the edge of the copper (Cu) grid on which the amorphous carbon foil is deposited as shown in Figure 28. Furthermore from SAED patterns several bright spots and rings are visible which cannot be attributed to β -MgH₂. These unidentified planes match with an FCC lattice with lattice parameter of 3.6 Å. Together with the observation that the particle number density and size increases significantly close to the Cu grid strongly suggests the formation of Cu nanoparticles. Unfortunately EDX cannot be utilized to lead to a decisive answer, as the Cu grid would always produce stray radiation. However, by using a silicon-nitride membrane the surface nucleation and growth of Cu nanoparticles could completely be prevented, indeed proving that the observed nanoparticles in Figure 28 stem from the Cu grid bars indicating that they can form at temperatures much lower than the melting temperature of copper (about 520 versus 1360 K).

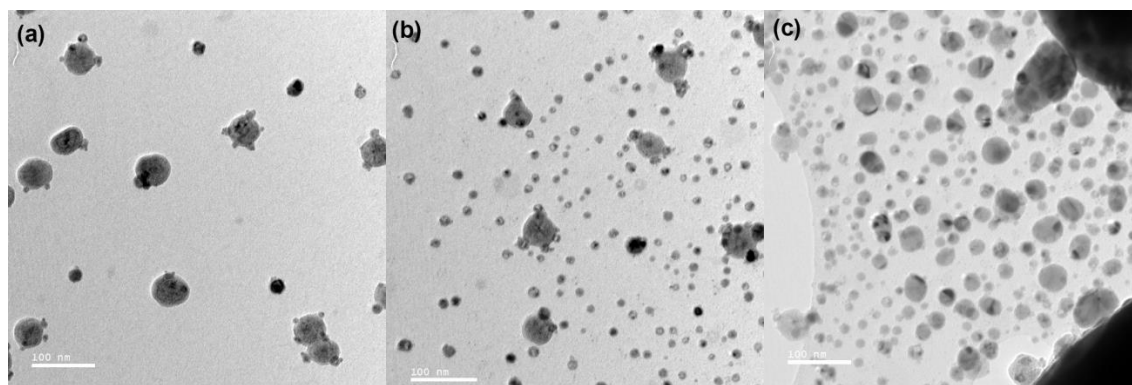


Figure 28: TEM bright field images of hydrogenated Mg-Ti nanoparticles at 250 °C for 2 hours. The images are taken (a) in the center (b) closer to the edge (c) near the edge of the window.

4.4 Dehydrogenation of Mg-Ti-H nanoparticles

Dehydrogenation of the hydrogenated nanoparticles has been carried out by two possible methods. Firstly, the nanoparticles could be heated in the hydrogenation setup at various molecular hydrogen gas pressures or evacuated to 10^{-2} mbar. The other method is to heat the nanoparticles in the TEM in a high vacuum environment of 10^{-7} mbar. According to the Van 't Hoff equation (Equation 4) the rutile MgH_2 will desorb hydrogen atoms at approximately 280°C under 1 bar H_2 . Therefore, hydrogenation was carried out at 300°C under 1 bar H_2 for 2 hours.

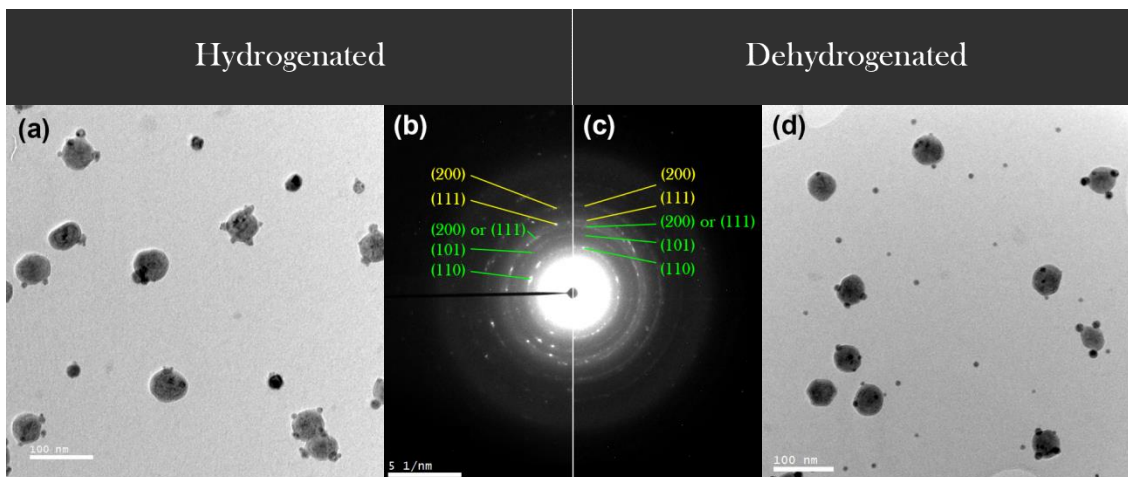


Figure 29: TEM bright field images of the (a,b) hydrogenated alloyed nanoparticles with its SAED pattern and (c,d) the hydrogenated nanoparticles after heating at 300°C at 1 bar H_2 for 2 hours. The MgH_2 and Cu planes are indexed in green and yellow, respectively.

Figure 29a shows hydrogenated alloyed Mg-Ti nanoparticles with Cu nanoparticle contamination as a side effect of the Cu support grids used. The SAED pattern (Figure 29b) corresponds to rutile MgH_2 as the low index $\{110\}$, $\{101\}$ and $\{200\}$ or $\{111\}$ planes are resolved. The nanoparticles are also shown after heating the nanoparticles for 2 hours at conditions that would desorb hydrogen predicted by the Van 't Hoff equation. Yet, no HCP Mg or HCP Ti could be identified from the SAED pattern (Figure 29c) such that dehydrogenation did not occur under these conditions. To increase the thermodynamic driving force for dehydrogenation the same particles were heated at 300°C for 3 hours at 10^{-2} mbar i.e. significantly lower than the equilibrium pressure of MgH_2 at 300°C . Yet, again, no hydrogen desorption could be identified based on the SAED pattern.

To investigate the effect of the structural motif of the nanoparticles, hydrogenated Ti-C-Mg core-shell nanoparticles were dehydrogenated subjected to the same conditions i.e. heating at 300°C at 10^{-2} mbar for 3 hours. The result is shown in Figure 30. Under these circumstances the surface nucleation rate of the contaminating Cu nanoparticles is substantially higher. Possibly, the Cu support grid evaporates more Cu to establish its vapour pressure, which subsequently condensates and nucleates on the substrate. Furthermore, the surface nucleated Cu nanoparticles seem to react with the Mg-Ti nanoparticles as the MgO shell has signs of corrosion in the form of cracks (top right nanoparticle in Figure 30d). Even though the MgO shell appears to be cracked, no hydrogen desorption is observed. In literature often an activation step for hydrogen absorption and desorption is mentioned to be required, otherwise no hydrogenation cycles could be achieved. The activation step consist of several high temperature cycles up to 400°C under a hydrogen gas atmosphere [14], [24]. The result of the activation step is presumed to be the cracking of the MgO surface passivation layer due to thermal expansion. However, to the best of the author's knowledge no TEM images (or other direct proofs)

support this hypothesized mechanism. Moreover, no dehydrogenation occurs even though the MgO surface shell appears to be cracked such that bare MgH₂ is exposed. Hence, this observation does not agree with the published literature e.g. [63], [64].

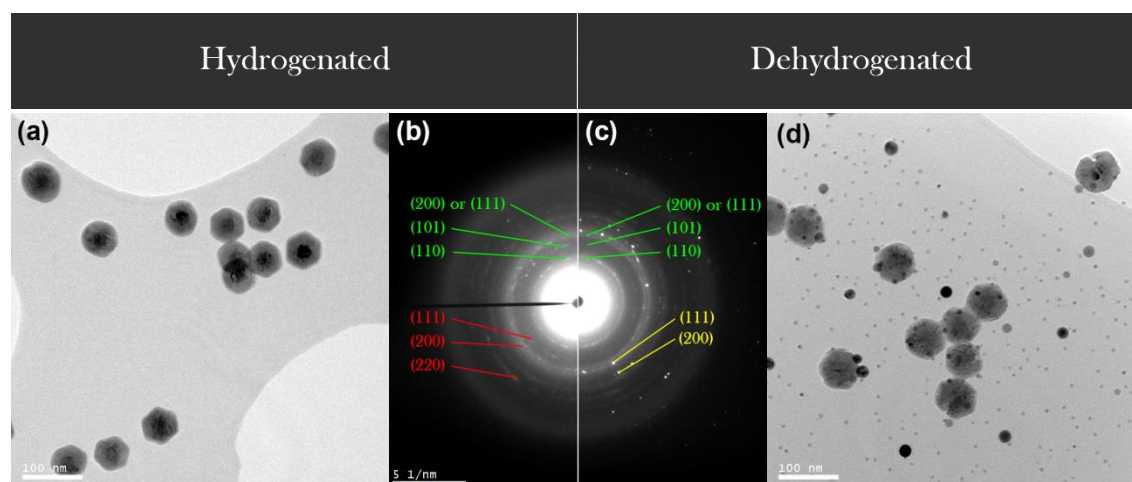


Figure 30: TEM bright field images and the SAED pattern for (a,b) hydrogenated core-shell nanoparticles (c,d) after heating at 300 °C at 10⁻² mbar for 3 hours. The MgH₂, TiC and Cu planes are indexed in green, red and yellow, respectively.

More interestingly, the structural motif of the initially core-shell nanoparticles has vanished after the dehydrogenation process. After vacuum heating at 300 °C the particles have formed an alloyed structure. In the SAED pattern the {101} MgH₂ reflection has lost intensity whereas a new interplanar distances appeared with increased intensity at 2.24±0.02 Å and 2.09±0.02 Å. Possibly, several forbidden reflection for the rutile structure have appeared due to a reduction in symmetry. As the reflection at 2.24±0.02 Å and 2.09±0.02 Å can be indexed by {111} and {210} of the rutile MgH₂ lattice, respectively. However, these reflections overlap with the {111} and {200} reflections of Cu. Most likely the reflection originate from Cu contamination as in the SAED pattern there are several bright spots at {111} and {200} of Cu. Yet, due to the overlapping reflections, the origin is not certain.

More stringent conditions were imposed on the hydrogenated nanoparticles by heating them in high vacuum in the TEM. Under these conditions there is a large thermodynamic driving force for hydrogen desorption, since the pressure is many orders of magnitude below the hydrogen equilibrium pressure. Thermal energy is only required to provide sufficient energy to overcome several barriers during the desorption processes. During TEM heating at 300 °C for 60 minutes no phase transition or void formation occurred for the alloyed Mg-Ti nanoparticles shown in Figure 31. Therefore, the temperature was increased to 325 °C and the nanoparticles where heated for 30 minutes. Yet again, void formation and hydrogen desorption did not occur. Further increasing the temperature to 350 °C and 375 °C also was not sufficient as well to observe hydrogen desorption. The SAED pattern and the bright field TEM images remained identical during the heating in high vacuum as shown in Figure 31.

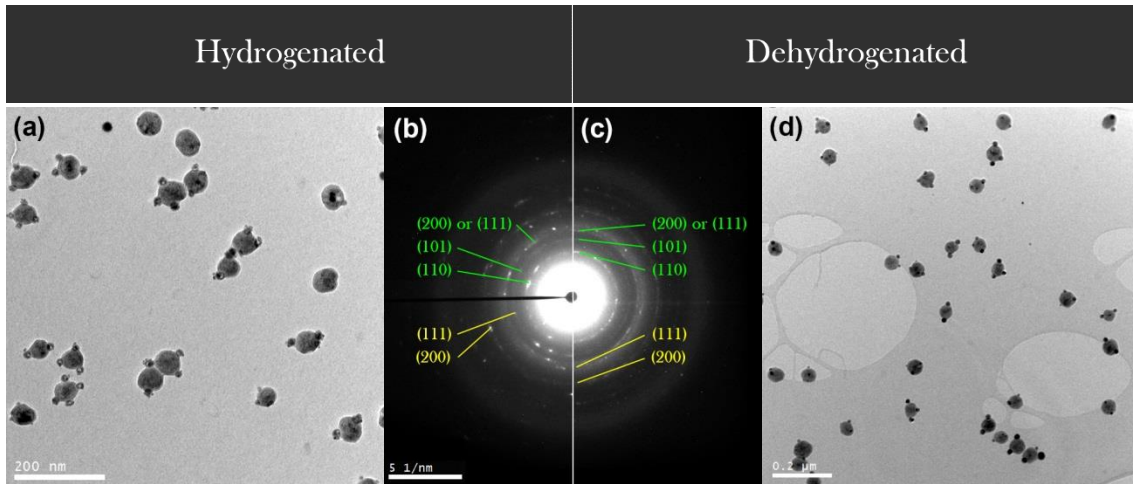


Figure 31: TEM bright field images and the SAED pattern for (a,b) hydrogenated alloyed nanoparticles (c,d) after heating for 2.5 hours up to 375 °C in high vacuum. The MgH_2 and Cu planes are indexed in green and yellow, respectively.

To attempt to improve hydrogen sorption kinetics, the Ti-rich nanoparticles synthesized in $Ar-H_2$ were heated in TEM. The nanoparticles produced with hydrogen have a TiH_2 crystal structure of $4.45 \pm 0.05 \text{ \AA}$ which increased to $4.86 \pm 0.05 \text{ \AA}$ as a result of hydrogenation. Initially the nanoparticles were heated at 300 °C for 30 minutes. However, this heating did not yield hydrogen desorption as observed from the SAED pattern. Further increasing the temperature to 350 °C for 30 minutes and 400 °C for 20 minutes also did not affect the nanoparticles, as shown in Figure 32. Even under these severe conditions the fluorite hydride structure is not capable of desorbing hydrogen. While void formation occurs rapidly during hydrogenation carried out at low temperatures, void formation due to Mg evaporation is completely suppressed due to the hydride phase present. Similar results are obtained when heating the nanoparticles with a TiC core starting at 300 °C and up to 400 °C for 20 minutes. The nanoparticles are too large for finite size effect to affect the thermodynamics of the system as predicted for pure Mg nanoclusters [9]. This implies that there are severe kinetic limitations among the hydrogen desorption processes that virtually block any hydrogen desorption.

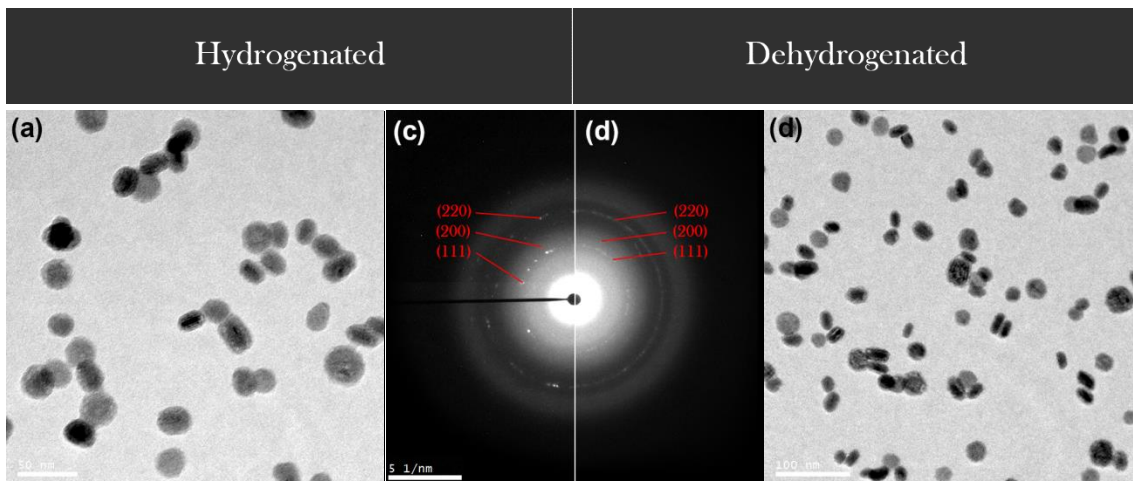


Figure 32: TEM bright field images and the SAED pattern for (a,b) hydrogenated Ti-rich nanoparticles (c,d) after heating for 1.5 hours up to 400 °C in high vacuum. TiH_2 planes are indexed in red.

Most likely the reason for blocking hydrogen desorption is a combination of the poor diffusion in the hydride and the MgO shell which completely encloses the nanoparticle. The hydride is a thermodynamically unfavourable state when the hydrogen pressure is below its equilibrium pressure, such that nucleation of HCP Mg is desired. Possible locations for nucleation of the HCP Mg phase are the interfaces with MgO and TiC/TiH₂ as generally heterogeneous nucleation requires less energy than homogeneous nucleation. Nucleation of HCP Mg requires transport of atomic hydrogen by means of diffusion through the MgH₂ lattice, followed by diffusion through the MgO shell. The rutile MgH₂ is known for its poor hydrogen diffusion rate which is the origin of the asymmetry in the hydrogen absorption and desorption processes. If the MgH₂ lattice is completely saturated with atomic hydrogen, the hydrogen transport through the hydride is greatly suppressed due to the low diffusion rate. In this case no vacant sites for atomic hydrogen are available such that diffusion by vacancy exchange is negligible. Hence, typically the desorption process is limited by the speed of the Mg/MgH₂ interface [65]. However, a virtue of nanoparticles is a small diffusion path length such that, despite the low diffusion coefficient, this can hardly be a rate limiting step. A more likely rate limiting step is related to the largely hydrogen impenetrable MgO shell [34]. By the low diffusion rate through the oxide shell the monolayer formation time of atomic hydrogen on the MgO shell is rather long. Subsequently, atomic hydrogen on the outside of the MgO shell needs to associate to form molecular hydrogen and detach from the surface. The association rate of two hydrogen atoms is proportional to the coverage of atomic hydrogen; hence this rate is dominated by the diffusion rate through the MgO shell.

The system studied in this thesis consists of isolated nanoparticles of which each is enclosed in 3-4 nm MgO shell which is formed *in-situ* during synthesis and grows during transport to the TEM. Due to the isolated nature large scale hydrogen absorption and desorption cannot occur in a collective manner e.g. only local phase transitions are possible. This is unlike compacted film of Mg-Ti nanoparticles or thin films which are physically connected and share a common oxide shell on top. Furthermore, these systems are synthesized, hydrogenated and dehydrogenated (while sampled by X-ray diffraction to monitor hydrogen uptake and release) in one vacuum system that prevents uncontrolled oxidation. In these cases, local hydrogen diffusion pathways through the common oxide (either through the oxide, dislocations or cracks) can result in a phase transition on a global scale due to the possible limited oxide thickness and physically connected system.

The MgO shell is the only common feature among the synthesized isolated Mg-Ti nanoparticles with a range of sizes (25 to 60 nm), composition (47 to 88 at% Mg), structural motifs (alloyed and core-shell), shapes (hexagonal pyramids and tetrahedral) and crystal structures (solid solution HCP Mg-Ti, core-shell FCC TiC- HCP Mg and FCC TiC or TiH₂). Hence, all results and observations of the present investigated system point to the presence of a kinetic barrier for hydrogen desorption from the nanoparticles that is most likely related to the hydrogen impenetrable MgO shell that encloses every nanoparticle.

5. Conclusions

Bimetallic Mg-Ti nanoparticles have been produced with high pressure magnetron sputtering. Homogeneous nucleation in an inert Ar gas environment does not occur at a sufficiently high rate and therefore impurities are required for heterogeneous nucleation. An oxidized target results in a stable nucleation rate, but due to rapid erosion of the thin surface film this stops after 15-20 minutes. The resulting nanoparticles have an alloyed structure with a small nucleus, determined from bright field TEM images and compositional measurements by EDX. In order to gain control over the nucleation rate, hydrogen or methane gas is introduced via a high precision leak valve in the aggregation chamber of the nanocluster source in addition to the Ar sputtering gas. The high nucleation rate is attributed to the high reactivity of the Ti vapour with carbon and hydrogen to form TiC and TiH₂, respectively. This directly impacts the growth sequence as these compounds are seeds for magnesium nucleation, such that in any case the nanoparticle has a core-shell structural motif. Due to the very well matching interplanar spacing of the FCC TiC core and HCP Mg shell a semi coherent interface is formed between the core and shell. The actual shape and facets of the Mg-rich nanoparticles are determined based on SAED patterns and 3D reconstruction based on a tilt series (tomography). The shape of Mg-Ti nanoparticles corresponds to a truncated hexagonal pyramid and deviates from a hexagonal prism for pure Mg nanoparticles. The different shape is explained by assuming the presence of Ti in the shell, despite not having direct evidence in terms of elemental mapping. When the Mg concentration is reduced, the FCC TiC or FCC TiH₂ core forces the entire particle to acquire the FCC crystal structure *in-situ*, such that no HCP Mg is identifiably in the SAED pattern. Due to the high reactivity of Mg with respect to oxygen, all particles are enclosed by a 3-4 nm MgO shell. Consequently, when the particle become smaller and smaller MgO formation consumes nearly all Mg, which results in void development inside the nanoparticle. In order to minimize the fraction of Mg loss due to oxidation the particles should be relatively large. This restricts the size of any bimetallic Mg nanoparticles to sizes above approximately 25 nm. Achieving finite size effects is therefore impossible with gas phase synthesized Mg-Ti nanoparticles, as this requires sizes well below 25 nm.

Evaporation of Mg during hydrogenation is not suppressed in Mg-Ti nanoparticles. At low temperatures (below 150 °C) no hydride is formed and Mg evaporation leads to clustering of voids. Only at higher temperatures (above 200 °C) the hydride formation is sufficiently fast and Mg evaporation can be prevented. The sequence of hydrogen absorption can be regarded as a simple one dimensional potential landscape that contains several barriers. Only at higher temperatures a sufficiently high absorption rate can be achieved. In this case the hydride formation first results in an MgH₂ shell that acts as a diffusion barrier for Mg which limits evaporation. Compositional tuning of the hydride crystal structure is possible by adjusting the sectioned target. Even though no perfect alloying occurs, the crystal structures can be rutile MgH₂ or fluorite TiH₂ for Mg-rich and Ti-rich nanoparticles, respectively. This result is consistent with literature for thin films although the transition occurs in a Ti-rich composition due to the difficulty to form alloyed structures.

Desorption of hydrogen is predicted to occur around 280 °C under a hydrogen pressure of 1 bar or lower. Reducing the hydrogen pressure or increasing the temperature increases the thermodynamic driving force exponentially as described by the Van 't Hoff equation (Equation 4). Several attempts of hydrogen desorption have been carried out ranging from 300 °C at 1 bar hydrogen to 400 °C in high

vacuum conditions. Despite these stringent conditions which imposes a severe thermodynamic driving force for hydrogen desorption on the nanoparticles, no hydrogen desorption is observed. This strongly indicates the presence of kinetic barriers, probably most dominantly related to the MgO shell, among the processes for hydrogen desorption. Therefore, gas phase synthesized Mg-Ti nanoparticles are unsuitable for hydrogen storage purposes in their present form.

6. Future research and recommendations

In this thesis the characteristics of Mg-Ti nanoparticles for hydrogen storage purposes have been analysed, where hydrogen desorption could not be achieved under any circumstances. To improve the hydrogen desorption, or sorption in general, of Mg-Ti nanoparticles several options are still to be investigated. Titanium can be functionalized as a hydrogen dissociation catalyst. However, alloying of Mg and Ti is required to achieve this. In this work no purely alloyed Mg-Ti nanoparticles are synthesized, as TiC or TiH₂ is always forming a seed for Mg nucleation as a consequence of injection of methane or hydrogen gas, respectively. Clearly, no methane gas should be used during synthesis as TiC formation simply results in material loss for hydrogen storage. Furthermore, alloying of TiH₂ and Mg has been published several times for thin film systems [22], [59]. Therefore, the influence of hydrogen gas on the Mg-Ti nanoparticles should be further investigated. Previous work has shown that tuning of the structural motif of gas phase synthesized bimetallic nanoparticles of two bulk immiscible materials is possible [15]. Hence, possibly a similar result is feasible for Mg-Ti nanoparticles. Otherwise, the formation of a compact thin film of nanoparticles could provide an increased hydrogen diffusion rate through the oxide via more possible pathways (cracks, dislocations, grain boundaries) such that the hydrogen sorption kinetics are less limited by the enclosing MgO shell.

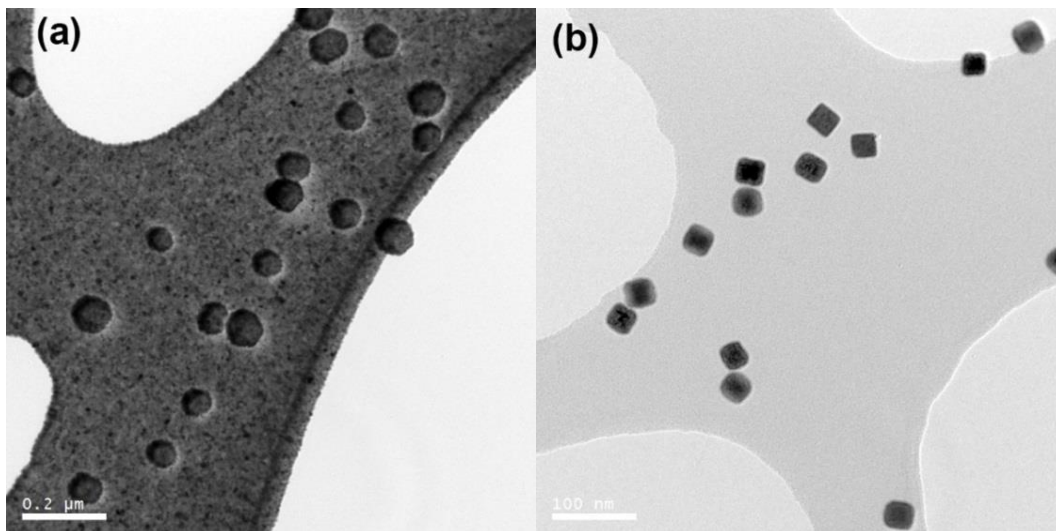


Figure 33: Using Pd in the Mg-Ti nanoparticle system. (a) Deposition of a thin film of Pd on top of the Mg-Ti nanoparticles (b) ternary Mg-Ti-Pd nanoparticles.

Alternatively, an external material can be deposited as a molecular hydrogen dissociation catalyst e.g. Pd. For example, a thin film of Pd has been deposited on Mg-Ti nanoparticles as shown in Figure 33a. This is a typical method that is applied for thin film systems where a several nm thick Pd film is deposited on top of the system. This film acts as a gateway for atomic hydrogen to the Mg-Ti nanoparticles such that the limiting effect of dissociation of hydrogen is excluded. Moreover, the Pd top-layer also helps preventing oxidation of the lower Mg-Ti layer(s).

A more elegant method is to incorporate Pd in the nanoparticle itself. This can be achieved by using a ternary sectioned target in the nanocluster source, as shown in Figure 33b. However, oxidation of Mg cannot be prevented such that clever growing conditions are required to obtain nanoparticles with suitable properties that are not hindered by an MgO shell. By choosing proper synthesis parameters, it might be possible to segregate Pd to the outside of the nanoparticle. Therefore, each particle contains a small amount of catalyst that does not require a relatively large amount of Pd as is needed in the case of a thin film.

Acknowledgements

During my time in the Nanostructured Materials and Interfaces (NMI) group I had the opportunity to work on a nanotechnological solution for present-day applications in the field of renewable energy. I could not only apply the knowledge I gathered for the past few years, but also developed practical skills by learning to operate a transmission electron microscope and understanding the high pressure magnetron sputtering nanocluster source. First of all, I would like to thank prof. dr. ir. Bart Kooi for having me in the NMI group. Thank you for your supervision and your everlasting patience when learning the basic operation of a transmission electron microscopy. Thank you prof. dr. George Palasantzas for the supervision along with Bart. I appreciate the advice and suggestions not only on the physics of my research project, but also for more personal problems (with my car). I'd like to thank Gert ten Brink for introducing me to the home-modified nanocluster source. Thank you for your advice during synthesis and all the interesting discussion we had. Also I appreciate all the daily support you gave regarding practical issues and data analysis. Thirdly, thanks to dr. Kèvin Knoops from the Molecular Cell Biology group for spending a couple of days of obtaining and teaching me to construct 3D reconstructed images of the nanoparticles. At last, I would like to thank the entire group for giving me a good time (especially the good times when we were treated with cake).

Appendix

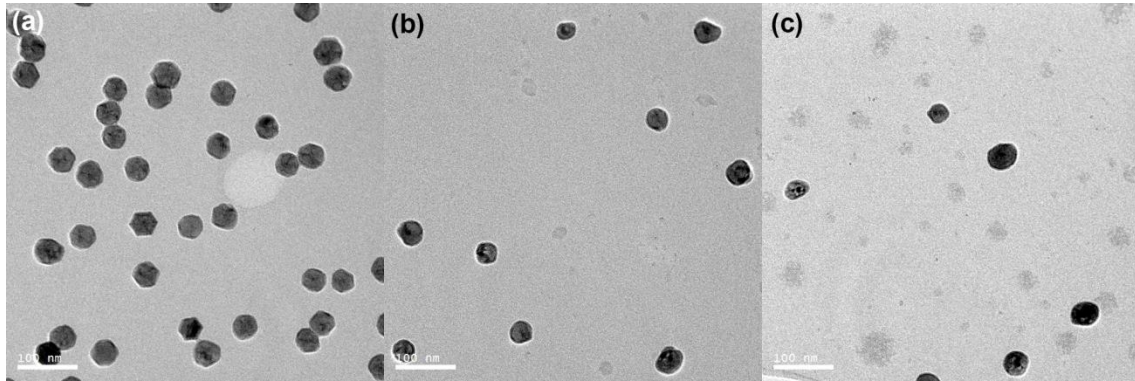


Figure A1: The Mg-Ti nanoparticles made in the range of (a) 5-15 minutes (b) 25-35 min (c) 45-55 min. Note that nanoparticle size is fairly similar, but number density is much lower. Also island growth seems to occur in (b) and (c).

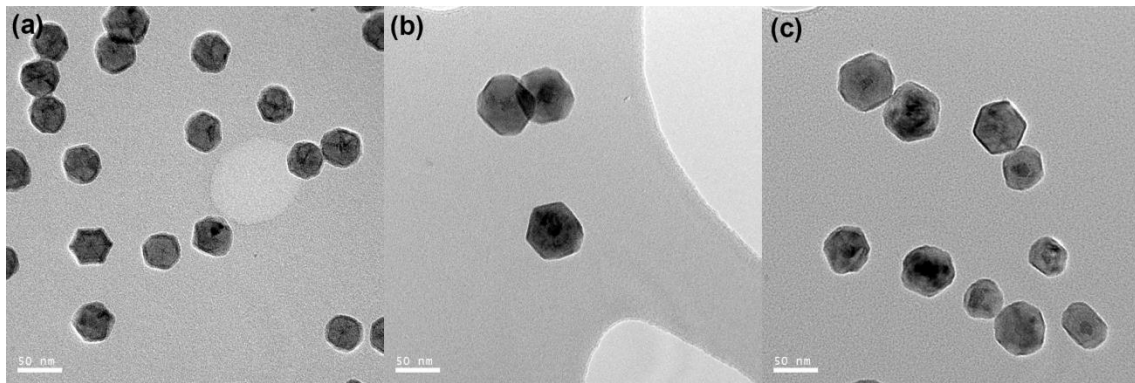


Figure A2: $Mg_{88}Ti_{12}$ nanoparticles synthesized in a pure Ar atmosphere, where the structural motif ranges from (a) alloyed nanoparticles to (b,c) more prominent core-shell nanoparticles.

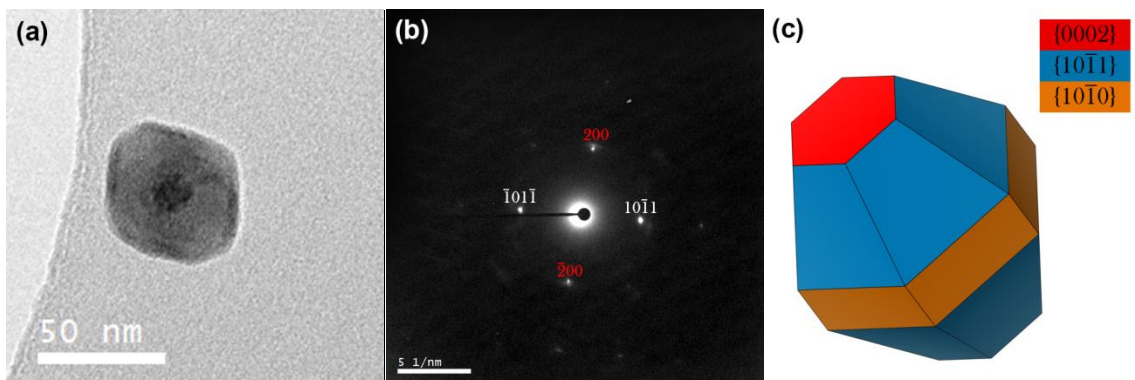


Figure A3: (a) High magnification bright field TEM image of a core-shell $Mg_{85}Ti_{15}$ nanoparticle (b) with its corresponding SAED pattern where Mg and TiC planes are indexed in white and red, respectively. (c) The 3D model in the equal orientation.

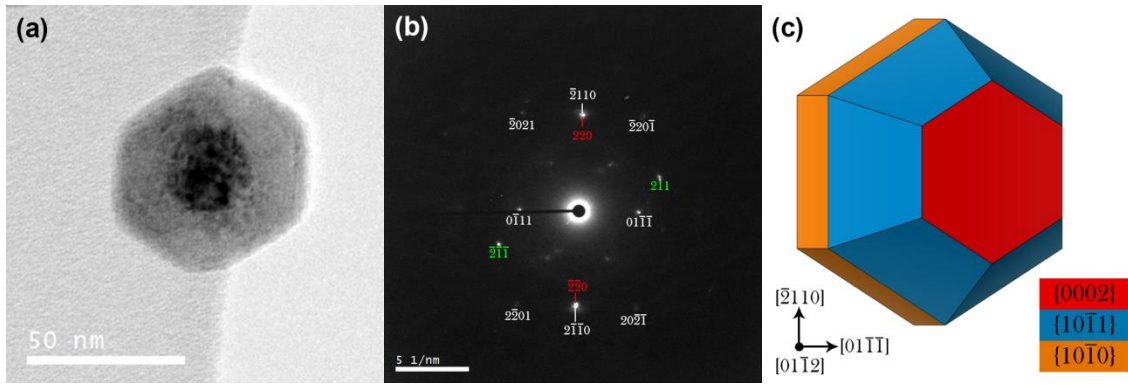


Figure A4: (a) High magnification bright field TEM image of a core-shell $\text{Mg}_{85}\text{Ti}_{15}$ nanoparticle after partial hydrogenation at $150\text{ }^{\circ}\text{C}$ for 2 hours (b) the corresponding SAED pattern along the $[01\bar{1}2]$ zone axis, where Mg, TiC and MgH_2 planes are indexed in white, red and green, respectively. Note that additional reflection occur at $\frac{1}{2}\{11\bar{2}0\}$ most likely due to reduced symmetry by hydrogen incorporation in the lattice. (c) The 3D model in the equal orientation.

References

- [1] N. Abas, A. Kalair, and N. Khan, "Review of fossil fuels and future energy technologies," *Futures*, vol. 69, pp. 31–49, May 2015.
- [2] A. Midilli, M. Ay, I. Dincer, and M. A. Rosen, "On hydrogen and hydrogen energy strategies: I: current status and needs," *Renew. Sustain. Energy Rev.*, vol. 9, no. 3, pp. 255–271, Jun. 2005.
- [3] M. Azhar Khan, M. Zahir Khan, K. Zaman, and L. Naz, "Global estimates of energy consumption and greenhouse gas emissions," *Renew. Sustain. Energy Rev.*, vol. 29, pp. 336–344, Jan. 2014.
- [4] R. Zacharia and S. ullah Rather, "Review of Solid State Hydrogen Storage Methods Adopting Different Kinds of Novel Materials," *J. Nanomater.*, vol. 2015, Oct. 2015.
- [5] L. Schlapbach and A. Züttel, "Hydrogen-storage materials for mobile applications," *Nature*, vol. 414, no. 6861, pp. 353–358, Nov. 2001.
- [6] A. Züttel, A. Remhof, A. Borgschulte, and O. Friedrichs, "Hydrogen: the future energy carrier," *Philos. Trans. R. Soc. Lond. Math. Phys. Eng. Sci.*, vol. 368, no. 1923, pp. 3329–3342, Jul. 2010.
- [7] A. Züttel, "Materials for hydrogen storage," *Mater. Today*, vol. 6, no. 9, pp. 24–33, Sep. 2003.
- [8] P. Selvam, B. Viswanathan, C. S. Swamy, and V. Srinivasan, "Magnesium and magnesium alloy hydrides," *Int. J. Hydrog. Energy*, vol. 11, no. 3, pp. 169–192, 1986.
- [9] R. W. P. Wagemans, J. H. van Lenthe, P. E. de Jongh, A. J. van Dillen, and K. P. de Jong, "Hydrogen Storage in Magnesium Clusters: Quantum Chemical Study," *J. Am. Chem. Soc.*, vol. 127, no. 47, pp. 16675–16680, Nov. 2005.
- [10] G. Krishnan, B. J. Kooi, G. Palasantzas, Y. Pivak, and B. Dam, "Thermal stability of gas phase magnesium nanoparticles," *J. Appl. Phys.*, vol. 107, no. 5, p. 53504, Mar. 2010.
- [11] Y. Yin, R. M. Rioux, C. K. Erdonmez, S. Hughes, G. A. Somorjai, and A. P. Alivisatos, "Formation of Hollow Nanocrystals Through the Nanoscale Kirkendall Effect," *Science*, vol. 304, no. 5671, pp. 711–714, Apr. 2004.
- [12] B. J. Kooi, G. Palasantzas, and J. T. M. D. Hosson, "Gas-phase synthesis of magnesium nanoparticles: A high-resolution transmission electron microscopy study," *Appl. Phys. Lett.*, vol. 89, no. 16, p. 161914, Oct. 2006.
- [13] M. Pozzo and D. Alfè, "Hydrogen dissociation and diffusion on transition metal (= Ti, Zr, V, Fe, Ru, Co, Rh, Ni, Pd, Cu, Ag)-doped Mg(0001) surfaces," *Int. J. Hydrog. Energy*, vol. 34, no. 4, pp. 1922–1930, Feb. 2009.
- [14] A. Zaluska, L. Zaluski, and J. O. Ström–Olsen, "Nanocrystalline magnesium for hydrogen storage," *J. Alloys Compd.*, vol. 288, no. 1–2, pp. 217–225, Jun. 1999.
- [15] G. Krishnan, M. A. Verheijen, G. H. ten Brink, G. Palasantzas, and B. J. Kooi, "Tuning structural motifs and alloying of bulk immiscible Mo–Cu bimetallic nanoparticles by gas-phase synthesis," *Nanoscale*, vol. 5, no. 12, pp. 5375–5383, Jun. 2013.
- [16] G. Krishnan, R. F. Negrea, C. Ghica, G. H. ten Brink, B. J. Kooi, and G. Palasantzas, "Synthesis and exceptional thermal stability of Mg-based bimetallic nanoparticles during hydrogenation," *Nanoscale*, vol. 6, no. 20, pp. 11963–11970, Sep. 2014.
- [17] K. Asano, H. Enoki, and E. Akiba, "Synthesis of HCP, FCC and BCC structure alloys in the Mg–Ti binary system by means of ball milling," *J. Alloys Compd.*, vol. 480, no. 2, pp. 558–563, Jul. 2009.
- [18] K. Asano, H. Enoki, and E. Akiba, "Synthesis of Mg–Ti FCC hydrides from Mg–Ti BCC alloys," *J. Alloys Compd.*, vol. 478, no. 1–2, pp. 117–120, Jun. 2009.
- [19] H. Imamura, K. Masanari, M. Kusuhara, H. Katsumoto, T. Sumi, and Y. Sakata, "High hydrogen storage capacity of nanosized magnesium synthesized by high energy ball-milling," *J. Alloys Compd.*, vol. 386, no. 1–2, pp. 211–216, Jan. 2005.
- [20] A. Baldi, M. Gonzalez-Silveira, V. Palmisano, B. Dam, and R. Griessen, "Destabilization of the Mg–H system through elastic constraints," *Phys. Rev. Lett.*, vol. 102, no. 22, p. 226102, Jun. 2009.

- [21] L. P. A. Mooij, A. Baldi, C. Boelsma, K. Shen, M. Wagemaker, Y. Pivak, H. Schreuders, R. Griessen, and B. Dam, "Interface Energy Controlled Thermodynamics of Nanoscale Metal Hydrides," *Adv. Energy Mater.*, vol. 1, no. 5, pp. 754–758, Oct. 2011.
- [22] K. Asano, R. J. Westerwaal, A. Anastasopol, L. P. A. Mooij, C. Boelsma, P. Ngene, H. Schreuders, S. W. H. Eijt, and B. Dam, "Destabilization of Mg Hydride by Self-Organized Nanoclusters in the Immiscible Mg–Ti System," *J. Phys. Chem. C*, vol. 119, no. 22, pp. 12157–12164, Jun. 2015.
- [23] D. M. Borsa, R. Gremaud, A. Baldi, H. Schreuders, J. H. Rector, B. Kooi, P. Vermeulen, P. H. L. Notten, B. Dam, and R. Griessen, "Structural, optical, and electrical properties of $Mg_yTi_{1-y}H_x$ thin films," *Phys. Rev. B*, vol. 75, no. 20, p. 205408, May 2007.
- [24] M. Calizzi, F. Venturi, M. Ponthieu, F. Cuevas, V. Morandi, T. Perkisas, S. Bals, and L. Pasquini, "Gas-phase synthesis of Mg–Ti nanoparticles for solid-state hydrogen storage," *Phys. Chem. Chem. Phys.*, vol. 18, no. 1, pp. 141–148, Dec. 2015.
- [25] M. Calizzi, D. Chericoni, L. H. Jepsen, T. R. Jensen, and L. Pasquini, "Mg–Ti nanoparticles with superior kinetics for hydrogen storage," *Int. J. Hydrog. Energy*.
- [26] T. Liu, C. Chen, F. Wang, and X. Li, "Enhanced hydrogen storage properties of magnesium by the synergistic catalytic effect of TiH_{1.971} and TiH_{1.5} nanoparticles at room temperature," *J. Power Sources*, vol. 267, pp. 69–77, Dec. 2014.
- [27] J. L. Murray, "The Mg–Ti (Magnesium-Titanium) system," *Bull. Alloy Phase Diagr.*, vol. 7, no. 3, pp. 245–248.
- [28] M. Dornheim, "Thermodynamics of Metal Hydrides: Tailoring Reaction Enthalpies of Hydrogen Storage Materials," in *Thermodynamics - Interaction Studies - Solids, Liquids and Gases*, J. C. Moreno Piraján, Ed. InTech, 2011.
- [29] M. Dornheim, S. Doppiu, G. Barkhordarian, U. Boesenberg, T. Klassen, O. Gutfleisch, and R. Bormann, "Hydrogen storage in magnesium-based hydrides and hydride composites," *Scr. Mater.*, vol. 56, no. 10, pp. 841–846, May 2007.
- [30] M. V. Lototskiy, V. A. Yartys, B. G. Pollet, and R. C. Bowman Jr., "Metal hydride hydrogen compressors: A review," *Int. J. Hydrog. Energy*, vol. 39, no. 11, pp. 5818–5851, Apr. 2014.
- [31] P. S. Rudman, "Hydrogen-diffusion-rate-limited hydriding and dehydriding kinetics," *J. Appl. Phys.*, vol. 50, no. 11, pp. 7195–7199, Nov. 1979.
- [32] B. Vigeholm, K. Jensen, B. Larsen, and A. S. Pedersen, "Elements of hydride formation mechanisms in nearly spherical magnesium powder particles," *J. Common Met.*, vol. 131, no. 1, pp. 133–141, Mar. 1987.
- [33] V. Bérubé, G. Radtke, M. Dresselhaus, and G. Chen, "Size effects on the hydrogen storage properties of nanostructured metal hydrides: A review," *Int. J. Energy Res.*, vol. 31, no. 6–7, pp. 637–663, Oct. 2006.
- [34] P. Hjort, A. Krozer, and B. Kasemo, "Hydrogen sorption kinetics in partly oxidized Mg films," *J. Alloys Compd.*, vol. 237, no. 1–2, pp. 74–80, Apr. 1996.
- [35] L. Zaluski, A. Zaluska, and J. O. Ström-Olsen, "Nanocrystalline metal hydrides," *J. Alloys Compd.*, vol. 253–254, pp. 70–79, May 1997.
- [36] A. Zaluska, L. Zaluski, and J. O. Ström-Olsen, "Structure, catalysis and atomic reactions on the nano-scale: a systematic approach to metal hydrides for hydrogen storage," *Appl. Phys. A*, vol. 72, no. 2, pp. 157–165, Feb. 2001.
- [37] P. J. Kelly and R. D. Arnell, "Magnetron sputtering: a review of recent developments and applications," *Vacuum*, vol. 56, no. 3, pp. 159–172, Mar. 2000.
- [38] C. H. Shon and J. K. Lee, "Modeling of magnetron sputtering plasmas," *Appl. Surf. Sci.*, vol. 192, no. 1–4, pp. 258–269, May 2002.
- [39] B. Chapman, *Glow Discharge Processes*. John Wiley & Sons, 1980.
- [40] P. Sigmund, "Theory of Sputtering. I. Sputtering Yield of Amorphous and Polycrystalline Targets," *Phys. Rev.*, vol. 184, no. 2, pp. 383–416, Aug. 1969.
- [41] B. M. Smirnov, *Cluster Processes in Gases and Plasmas*. John Wiley & Sons, 2009.
- [42] G. H. ten Brink, G. Krishnan, B. J. Kooi, and G. Palasantzas, "Copper nanoparticle formation in a reducing gas environment," *J. Appl. Phys.*, vol. 116, no. 10, p. 104302, Sep. 2014.

- [43] D. B. Williams and C. B. Carter, *Transmission Electron Microscopy: A Textbook for Materials Science*. Springer Science & Business Media, 2009.
- [44] G. Cao and Y. Wang, *Nanostructures and Nanomaterials: Synthesis, Properties, and Applications*. World Scientific, 2011.
- [45] K. C. Kim, B. Dai, J. K. Johnson, and D. S. Sholl, "Assessing nanoparticle size effects on metal hydride thermodynamics using the Wulff construction," *Nanotechnology*, vol. 20, no. 20, p. 204001, 2009.
- [46] D. Zhou, S. Jin, Y. Li, F. Qiu, F. Deng, J. Wang, and Q. Jiang, "Effect of stoichiometry on the surface energies of {100} and {111} and the crystal shape of TiCx and TiNx," *CrystEngComm*, vol. 15, no. 4, pp. 643–649, Dec. 2012.
- [47] D. E. Grove, U. Gupta, and A. W. Castleman, "Effect of Carbon Concentration on Changing the Morphology of Titanium Carbide Nanoparticles from Cubic to Cuboctahedron," *ACS Nano*, vol. 4, no. 1, pp. 49–54, Jan. 2010.
- [48] Y. Xiong, J. M. McLellan, J. Chen, Y. Yin, Z.-Y. Li, and Y. Xia, "Kinetically Controlled Synthesis of Triangular and Hexagonal Nanoplates of Palladium and Their SPR/SERS Properties," *J. Am. Chem. Soc.*, vol. 127, no. 48, pp. 17118–17127, Dec. 2005.
- [49] H. Guo, Y. Chen, H. Ping, L. Wang, and D.-L. Peng, "One-pot synthesis of hexagonal and triangular nickel–copper alloy nanoplates and their magnetic and catalytic properties," *J. Mater. Chem.*, vol. 22, no. 17, p. 8336, 2012.
- [50] G. Zhang, J. B. Jasinski, J. L. Howell, D. Patel, D. P. Stephens, and A. M. Gobin, "Tunability and stability of gold nanoparticles obtained from chloroauric acid and sodium thiosulfate reaction," *Nanoscale Res. Lett.*, vol. 7, no. 1, pp. 1–9, Jun. 2012.
- [51] V. Germain, J. Li, D. Ingert, Z. L. Wang, and M. P. Pileni, "Stacking Faults in Formation of Silver Nanodisks," *J. Phys. Chem. B*, vol. 107, no. 34, pp. 8717–8720, Aug. 2003.
- [52] J.-E. Sundgren, B.-O. Johansson, and S.-E. Karlsson, "Mechanisms of reactive sputtering of titanium nitride and titanium carbide I: Influence of process parameters on film composition," *Thin Solid Films*, vol. 105, no. 4, pp. 353–366, Jul. 1983.
- [53] J.-E. Sundgren, B.-O. Johansson, S.-E. Karlsson, and H. T. G. Hentzell, "Mechanisms of reactive sputtering of titanium nitride and titanium carbide II: Morphology and structure," *Thin Solid Films*, vol. 105, no. 4, pp. 367–384, Jul. 1983.
- [54] O. A. Fouad, A. K. Rumaiz, and S. I. Shah, "Reactive sputtering of titanium in Ar/CH₄ gas mixture: Target poisoning and film characteristics," *Thin Solid Films*, vol. 517, no. 19, pp. 5689–5694, Aug. 2009.
- [55] S. R. Shatynski, "The thermochemistry of transition metal carbides," *Oxid. Met.*, vol. 13, no. 2, pp. 105–118.
- [56] W.-E. Wang, "Thermodynamic evaluation of the titanium-hydrogen system," *J. Alloys Compd.*, vol. 238, no. 1, pp. 6–12, May 1996.
- [57] P. Vermeulen, P. C. J. Graat, H. J. Wondergem, and P. H. L. Notten, "Crystal structures of Mg_yTi_{100-y} thin film alloys in the as-deposited and hydrogenated state," *Int. J. Hydrog. Energy*, vol. 33, no. 20, pp. 5646–5650, Oct. 2008.
- [58] J. Nguyen, N. Glandut, C. Jaoul, and P. Lefort, "Hydrogen insertion in substoichiometric titanium carbide," *Int. J. Hydrog. Energy*, vol. 40, no. 27, pp. 8562–8570, Jul. 2015.
- [59] A. Baldi, R. Gremaud, D. M. Borsa, C. P. Baldé, A. M. J. van der Eerden, G. L. Kruijtzter, P. E. de Jongh, B. Dam, and R. Griessen, "Nanoscale composition modulations in Mg_yTi_{1-y}H_x thin film alloys for hydrogen storage," *Int. J. Hydrog. Energy*, vol. 34, no. 3, pp. 1450–1457, Feb. 2009.
- [60] S. Er, D. Tiwari, G. A. de Wijs, and G. Brocks, "Tunable hydrogen storage in magnesium-transition metal compounds: First-principles calculations," *Phys. Rev. B*, vol. 79, no. 2, p. 24105, Jan. 2009.
- [61] P. Vermeulen, R. A. H. Niessen, and P. H. L. Notten, "Hydrogen storage in metastable Mg_yTi_(1-y) thin films," *Electrochem. Commun.*, vol. 8, no. 1, pp. 27–32, Jan. 2006.

- [62] P. Vermeulen, H. J. Wondergem, P. C. J. Graat, D. M. Borsa, H. Schreuders, B. Dam, R. Griessen, and P. H. L. Notten, "In situ electrochemical XRD study of (de)hydrogenation of Mg_yTi_{100-y} thin films," *J. Mater. Chem.*, vol. 18, no. 31, pp. 3680–3687, Jul. 2008.
- [63] S. Kumar, V. Singh, C. Cassidy, C. Pursell, C. Nivargi, B. Clemens, and M. Sowwan, "Hydrogenation of Mg nanofilms catalyzed by size-selected Pd nanoparticles: Observation of localized MgH_2 nanodomains," *J. Catal.*, vol. 337, pp. 14–25, May 2016.
- [64] A. Borgschulte, M. Biemann, A. Züttel, G. Barkhordarian, M. Dornheim, and R. Bormann, "Hydrogen dissociation on oxide covered MgH_2 by catalytically active vacancies," *Appl. Surf. Sci.*, vol. 254, no. 8, pp. 2377–2384, Feb. 2008.
- [65] C. M. Stander, "Kinetics of decomposition of magnesium hydride," *J. Inorg. Nucl. Chem.*, vol. 39, no. 2, pp. 221–223, Jan. 1977.